Journal of Materials Research and Technology 37 (2025) 5265–5282

Contents lists available at ScienceDirect

Journal of Materials Research and Technology

journal homepage: www.elsevier.com/locate/jmrt

Evaluation of high-temperature wear behaviour of selective laser melted 17-4 PH stainless steel through laser shock peening

S. Pradeep Kumar [a], N. Radhika [a,*], P. Dinesh Babu [b], T. Ram Prabhu [c], Jaiprakash Gautam [d], V. Chakkravarthy [e]

[a] Department of Mechanical Engineering, Amrita School of Engineering, Coimbatore, Amrita Vishwa Vidyapeetham, India
[b] School of Mechanical Engineering, SASTRA Deemed University, Thanjavur, India
[c] CEMILAC, Defence R&D Organization, Bangalore, India
[d] School of Engineering Sciences and Technology, University of Hyderabad, Hyderabad, India
[e] Welding and Additive Manufacturing Centre, Cranfield University, Bedford, United Kingdom

ARTICLE INFO

Keywords:
Metal additive manufacturing
17-4 PH stainless steel
Laser shock peening
High temperature wear

ABSTRACT

This study investigates the high-temperature wear resistance of laser shock peened (LSP) 17-4 precipitation-hardened stainless steel fabricated via selective laser melting (SLM), addressing the critical need for enhanced surface durability in elevated-temperature conditions. Four material conditions were analysed: as-printed (AP), heat-treated (AP + HT), laser shock peened (AP + LSP), and both treatments combined (AP + HT + LSP). Wear tests using a pin-on-disc setup were conducted at room temperature (RT), 150 °C, 250 °C, and 350 °C. The AP + LSP condition consistently exhibited the lowest wear, attributed to the introduction of compressive residual stresses, severe plastic deformation, and strain hardening. In contrast, AP + HT and AP + HT + LSP suffered higher wear due to oxidation-assisted delamination and brittle morphology. At RT and 350 °C, AP + LSP achieved 34 % and 17 % lower wear rates than AP + HT, respectively. These findings highlight the effectiveness of LSP in enhancing the high-temperature tribological performance of SLM 17-4 PH stainless steel and offer valuable insights for its deployment in aerospace and energy applications.

1. Introduction

Although precipitation-hardened (PH) stainless steel (SS) offers excellent strength, wear resistance, and corrosion performance for critical applications, its poor machinability, especially after heat treatment, poses manufacturing challenges, making additive manufacturing a promising alternative for producing near-net shape components with minimal post-processing [1]. The 17-4 PH SS, fabricated through SLM, is gaining significant momentum in the Metal Additive Manufacturing (MAM) field due to its high strength, ductility, moderate corrosion resistance, customizable mechanical properties achievable through heat treatment, and ease of printability [2,3]. Key defects such as gas porosity, lack of fusion, keyhole pores, shrinkage, cavities, microstructural inhomogeneity, and anisotropy in three-dimensional (3D) printed components can be minimized using post-processing methods such as heat treatment, hot isostatic pressing (HIP), shot peening and so on [4,5]. Post-processing heat treatment like Solution/condition annealing (CA) heat treatment enhances the homogeneity of the microstructure in additively manufactured 17-4 PH SS samples, effectively mitigating micro-segregation while lowering the retained austenite content and Cr–Nb-rich precipitate formation [6]. During the SLM process, using argon as a chamber purging gas consistently produces fully martensitic 17-4 PH stainless steel, whereas the nitrogen environment retains more austenite in the matrix [7]. The authors, in their previous study [8,9], reported that the CA-H900 heat treatment enhanced the mechanical strength of 17-4 PH SS, despite the unavoidable presence of retained austenite [10].

Recent advancements in additive manufacturing have accelerated the integration of peening technologies, particularly LSP, as an addition to conventional heat treatment for enhancing the mechanical and wear performance of selective laser melted (SLMed) components [11,12]. LSP is distinguished by its ability to induce deep compressive residual stresses (CRS) without affecting surface roughness. Unlike traditional surface modification techniques, LSP introduces SPD without generating a heat-affected zone, thereby preserving the material's structural integrity [13–15]. This process enhances near-surface mechanical

* Corresponding author.
E-mail address: n_radhika1@cb.amrita.edu (N. Radhika).

https://doi.org/10.1016/j.jmrt.2025.07.164
Received 10 March 2025; Received in revised form 22 June 2025; Accepted 18 July 2025
Available online 18 July 2025
2238-7854/© 2025 The Authors. Published by Elsevier B.V. This is an open access article under the CC BY license (http://creativecommons.org/licenses/by/4.0/).

properties by imparting CRS, which improves hardness, strength, fatigue and wear resistance [16]. The mechanism involves high-energy shock-waves that induce localized plastic deformation, promoting the formation of nanoscale sub-grains and internal strain fields [17]. This results in a complex stress state within the surface layers, increasing dislocation density and enhancing microhardness. These characteristics establish LSP as a highly effective technique for optimizing the functional performance of SLMed materials, particularly in demanding engineering applications. Higher pulse density increased hardness and deepened the hardened layer by promoting grain refinement and stronger texture intensity [18]. However, it also led to increased surface roughness (Ra) due to a more pronounced peening pattern and SPD [19]. LSP alters the Ra by inducing localized remelting and plastic deformation, which smoothens the rough as-built surfaces in unpolished additive-manufactured alloys [20].

CA heat treatment of 3D printed samples at 1040 °C for 1 h promoted retained austenite formation and Nb- and Cr-rich carbide precipitation, while the primary wear mechanism in both as-printed and thermally treated specimens involved the formation and delamination of iron oxide and iron chromium oxide films [21]. The study reveals that load is the dominant factor influencing wear volume loss and specific wear rate in the dry sliding wear behaviour of 17-4 PH SS, with analysis of variance (ANOVA) analysis confirming its highest contribution, while Taguchi optimization technique identifies the optimal conditions for minimising wear. Adhesive and oxidative wear mechanisms were dominant in the worn-out surfaces of 17-4 PH SS [22]. In dry sliding wear tests, the 3D-printed 17-4 PH SS initially exhibited a steady-state coefficient of friction (CoF) of around 0.8 [23]. Additively manufactured 17-4 PH SS processed under the CA-H900 heat treatment condition exhibited a lower wear rate than conventionally manufactured 17-4 PH SS in dry conditions, regardless of the applied load, likely due to its higher hardness, with wear debris indicating pitting, surface fatigue, and oxidative wear [24]. RSM effectively predicts the coated sample's wear rate with a minimal error percentage [25]. In some cases, the conventional peak aging heat treatment did not improve the hardness of additively manufactured 17-4 PH SS due to the slow diffusion of Cu atoms in austenite. This inferior wear resistance behaviour after heat treatment was observed for a wide range of selective laser-melted materials, as it typically caused the material to wear out faster. In some cases, the conventional peak aging heat treatment did not improve the hardness of additively manufactured 17-4 PH SS due to the slow diffusion of Cu atoms in austenite. This inferior wear resistance behaviour after heat treatment was observed for a wide range of SLMed materials, as it typically caused the material to wear out faster [26]. In dry sliding wear tests, delamination was the dominant wear mechanism under high load conditions, characterized by the formation and subsequent detachment of the iron oxide film [21,27]. High-temperature conditions promoted the formation of a tribo-film, which acted as a protective layer on the surface [28]. High wear loss was observed at elevated temperatures due to the friction-induced failure of the brittle glaze layer [29]. LSP treatment altered the tensile residual stress (TRS) in additively manufactured 15-5 PH SS to beneficial compressive stress, increased surface micro-hardness by 13.07 %, and improved wear resistance by reducing the CoF and wear rate [1,16].

LSP has not been widely explored as a post-processing technique for AM components, and its impact on high-temperature wear behaviour remains largely unexamined. Moreover, research on the microstructural evolution, mechanical performance, and residual stress of AM 17-4 PH SS components is limited, particularly regarding enhancements from post-processing methods such as heat treatment and LSP. This study employs Response Surface Methodology (RSM) to optimize wear test conditions for a targeted wear rate in the as-printed state, enabling a precise evaluation of the material's wear resistance within the LSP-hardened layer, making it a novel approach in wear analysis. By systematically investigating the synergetic effects of heat treatment and LSP across various temperatures, this work provides novel insights into the potential of LSP as an advanced surface enhancement technique for improving the high-temperature wear resistance of additively manufactured 17-4 PH SS components operating in extreme environments.

2. Materials and methods

2.1. SLM Fabrication

The 17-4 PH SS cubic samples (20 × 20 × 20 mm) were fabricated using an EOS M280 SLM machine. The machine is equipped with a continuous wave (CW) 400 W ytterbium-fiber laser, which was used to melt gas-atomised 17-4 PH SS powder on a SS build plate. The chemical composition of the nitrogen gas atomised 17-4 PH SS powder is shown in Table 1. Cylindrical pins (30 mm in length and 10 mm in diameter) were fabricated using SLM for the dry sliding pin-on-disc wear test, as shown in Fig. 1. The optimal SLM process parameters, determined from the author's earlier work [1], were used to achieve high densification levels (>99.5 %). These parameters included a laser power of 220 W, a laser scanning velocity of 750 mm/s, a hatch spacing of 0.11 mm, a layer thickness of 40 μm, a horizontal build orientation, and a 67° angle rotating scanning strategy.

2.2. Heat treatment and LSP processing

The as-printed samples were subjected to condition annealing at 1040 °C for 30 min to dissolve all alloying elements in the solid solution state and to remove the residual stresses during the SLM process. Following solution annealing, peak aging (PA) was performed at 482 °C for 1 h, promoting the formation of fine copper-rich precipitates that enhance the material's mechanical strength. Fig. 2(a) shows the graphical representation of the CA-H900 heat treatment cycle. Before undergoing the LSP process, both the as-printed and heat-treated samples were fine-polished (Ra ≤0.2 μm). The LSP experiments were conducted using an indigenously developed electro-optic Q-switched Nd: YAG laser system. The system utilized a Q-switched Nd: YAG laser with specifications of 7 J pulse energy, a 5 Hz repetition rate, and a 10 ns pulse width. For this study, the laser energy was set to 3.5 J with a 3 mm spot diameter, achieving an overlap of 72 % over two passes (double peening). The flat-top laser profile ensured a uniform distribution of CRS. The LSP process was done on the surface parallel to the build direction (BD) for all samples, and the exposed surface will be subjected to the wear test. LSP enhances surface hardness by inducing CRS, which forms when the peak pressure generated surpasses the material's Hugoniot elastic limit (HEL). From the author's previous work [30], the energy density and peak pressure values for a single laser impact were calculated as 4.9514 GW/cm^2 and 3.152 GPa, respectively. Fig. 2(b) illustrates the schematic representation of the LSP principle, and Fig. 2 (c) shows the presence of microindentations on the laser shock-peened (LSPed) surface. Using RTEC MFT-5000 white light interferometer (WLI), the Ra of the polished and LSPed surfaces was measured before conducting the wear test. All pin samples were mirror-polished to a Ra below 0.3 μm. After peening, the Ra increased due to compressive stresses and dimple formation, as evident from Fig. 2(d). As reported by the authors in their previous work [9], mirror-polished Ra of the AP sample increased from 0.121 μm to 0.465 μm and the AP + HT sample increased from 0.271 μm to 0.569 μm after the LSP process. This slight increase in Ra comes from LSP dimples and introduced no microcracks or defects. Even though the LSP dents usually increase the Ra considerably, the overlapping strategy of the LSP process helped minimize them.

2.3. Microstructure, mechanical and wear behaviour

The microstructure, hardness and high-temperature wear tests were carried out on four types of samples, as listed out in Table 2.

The samples were etched using Fry's reagent for 20 s to expose the

Table 1
The chemical composition of the gas-atomised 17-4 PH SS powder.

Elemental composition	Ni	Cu	Cr	Mo	Si	Nb	P	C	Fe
17-4 PH SS powder (wt. %)	4.004	3.164	16.71	0.527	0.344	0.156	0.039	0.029	Balance

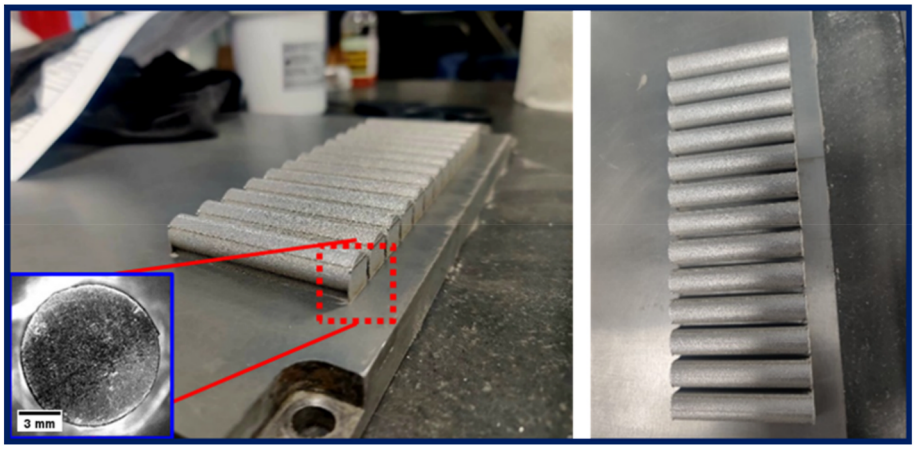


Fig. 1. 17-4 PH SS pin samples fabricated by the SLM process.

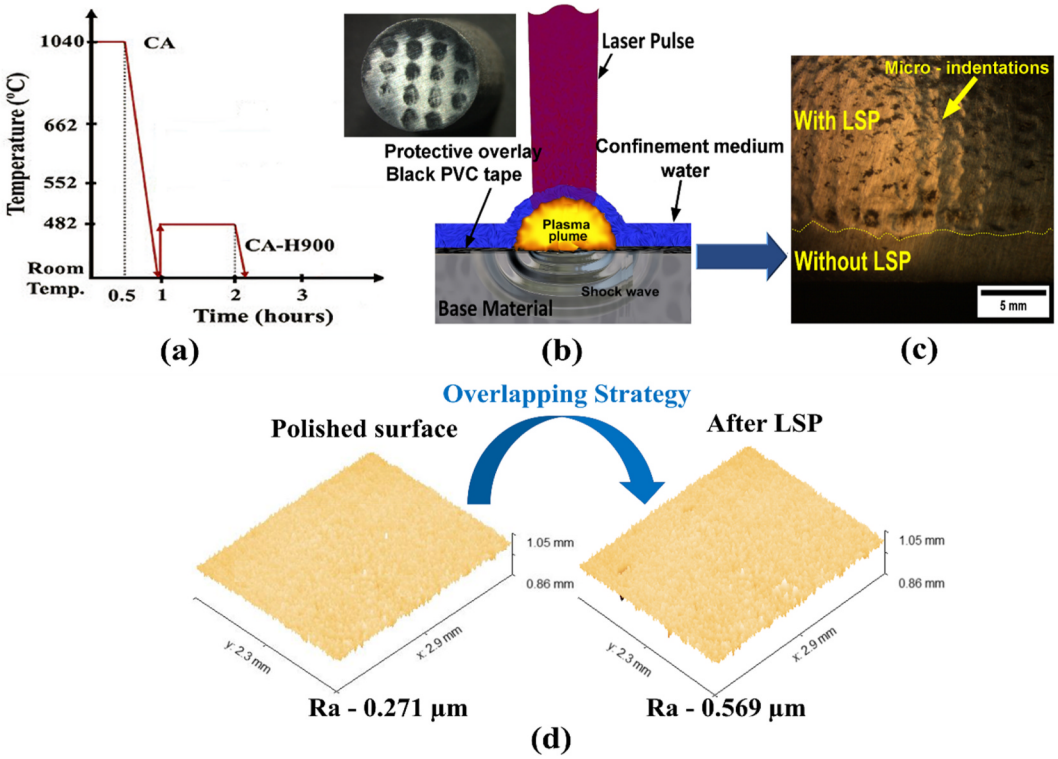


Fig. 2. Schematic representation of (a) CA-H900 heat treatment cycle, (b) LSP process, (c) Presence of micro-indentations, and (d) Surface roughness of polished and LSPed surface.

Table 2
Identification of experimental samples.

Sample details	Label
As printed	AP
As printed and heat treated (CA-H900)	AP + HT
As printed, followed by the LSP process	AP + LSP
As printed and heat treated, followed by the LSP process	AP + HT + LSP

grain boundaries [31]. Phase identification and texture analysis were performed with a Nova NanoSEM 450 equipped with an electron backscatter diffraction (EBSD) detector, using a step size of 0.2 µm. Electro-polishing was conducted using a Struers Lectropol 5 apparatus, with an electrolyte consisting of 100 mL perchloric acid and 900 mL ethanol. The process was carried out at −15 °C and 15 kV for 8 s. A Zeiss GeminiSEM 300 device was used for energy dispersive spectroscopy (EDS) analysis and field emission scanning electron microscopy

(FE-SEM) for analysing the microstructure and wear morphology. A Bruker diffractometer with CuKα radiation was used to gather X-ray diffraction (XRD) patterns for phase identification.

Microhardness was measured on polished cross-sections (surface perpendicular to BD) on peened samples using a Micro-Vickers Hardness tester (Tinius Olsen FH-006 series) with a 1 kgf (9.806 N) load and a dwell time of 10 s. Indentations were made at regular intervals of 50 μm from the surface down to a depth of 1300 μm, with spacing maintained based on one diagonal length of the indentation. Residual stresses were measured using a PROTO iXRD-MGR40P X-ray diffraction (XRD) system using the d-sin^{2}ψ method. A d versus sin^{2}ψ plot was constructed by monitoring the {211} crystallographic plane of the α-phase, observed at $2\theta = 82^{\circ}$, for eight different ψ angles. The top surface of the sample, which had been modified by the LSP process, was sequentially removed in controlled steps of approximately 50 μm using the electropolishing process. This step-by-step removal enabled access to the underlying subsurface regions of the LSP-affected zone. After each polishing step, diffraction scans were performed. This ensured that the residual stress measurements were taken at the same depth intervals as the hardness measurements.

The wear tests were conducted using a Novus Pin-on-Disc (POD) Tribometer, adhering to the ASTM G99-05 standard for dry sliding wear tests [32]. The disc material was EN 31 steel, with a hardness of 770 HV. Before peening, all pin samples were mirror-polished to a Ra below 0.3 μm. After peening, the Ra increased to 0.465 μm (AP + LSP) and 0.569 μm (AP + HT + LSP) due to dimple formation. The schematic diagram of the POD wear test machine is shown in Fig. 3. The wear rate and CoF were determined using standard equation (1) through (4), respectively.

$$Wear\ rate\ (mm^3/m) = \frac{Volume\ loss\ (mm^3)}{Sliding\ distance\ (m)} \tag{1}$$

$$Volume\ loss\ (mm^3) = \frac{Mass\ loss\ (g)}{Density\ (g/mm^3)} \tag{2}$$

$$Sliding\ distance\ (m) = \pi DNT \tag{3}$$

$$Coefficient\ of\ friction = \frac{Frictional\ force(N)}{Normal\ applied\ load(N)} \tag{4}$$

Where D represents the average diameter of the wear track (0.1 m), N denotes the rotational speed in revolutions per minute, and T indicates the duration in minutes.

An initial study using RSM was conducted on the AP sample to optimize the wear test parameters. The parameters varied in the study included Load (N), Sliding velocity (m/s), and Sliding distance (m), with the responses being volumetric wear rate (mm^3/m) and CoF. The responses corresponding to their respective process parameter ranges were entered into the Design Expert statistical software for analysis and optimization. The experimental results are based on the average values from three separate tests.

A subsequent validation study was conducted on the AP sample to assess the model's accuracy for optimization. These validated parameters were then applied for high-temperature wear testing across all four sample types. Subsequently, the pins underwent peak aging heat treatment and LSP. The front side of each pin in the LSP batch was subjected to double-peening to enhance surface properties before the wear testing. The tests were conducted at room temperature and elevated temperatures of 150 °C, 250 °C, and 350 °C, ensuring a comprehensive evaluation of wear performance under various thermal conditions. The wear track morphology of all four sample conditions was analysed to evaluate the extent and nature of the wear mechanisms involved.

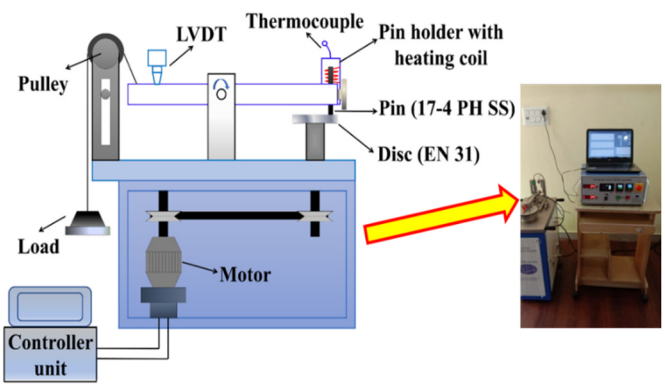


Fig. 3. Schematic diagram of the pin on disc tribometer.

3. Result and discussion

3.1. Microstructural Characterisation

Fig. 4 shows the optical microscopic (OM) images of the AP sample parallel to the build BD. The grain morphology shows the presence of directionally solidified columnar dendrites in the melt pool boundaries. The columnar grains are oriented towards the BD, as evident from Fig. 4 (a). A red rectangle highlights a specific region of interest, which is magnified to showcase the fine-grain morphology, as shown in Fig. 4(b). The lath martensitic microstructure exhibits refined columner grains attributed to the rapid solidification inherent in the SLM process. The fast cooling prevented the formation of austenite, while the higher Cr/Ni ratio ensured a complete transformation to martensite upon solidification.

Fig. 5(a) presents SEM images of the AP sample, revealing its microstructure along with the corresponding EDS line spectrum. Fig. 5 (b) illustrates the grain morphology of the AP + HT sample, accompanied by its EDS mapping. Fig. 5(c) highlights a high concentration of niobium (Nb), as confirmed by EDS analysis, which shows an Nb content of 14.16 %. This confirms the formation of Nb-rich precipitates, indicating the effectiveness of the heat treatment process. The presence of precipitates suggests their role in impeding dislocation movement, thereby contributing to a potential increase in hardness by Orowon strengthening.

Fig. 6(a) illustrates the microstructure of the AP + LSP sample, where crater formations are visible on the surface due to the intense shock waves generated during the LSP process. The topmost layer exhibits severely shattered and deformed grains, forming a severely deformed layer (SDL). Beneath this, a medium deformed layer (MDL) is observed, where the grain boundaries (GBs) begin to reappear. The melt pool boundary, characteristic of the 67° rotating scanning strategy, is outlined in the red line, with the region below it referred to as the lesser deformed layer (LDL). In Fig. 6(b), A similar microstructural response is observed in the AP + HT + LSP sample, where the SDL exhibits deformed grain boundaries at sub-cellular microstructure. However, the SDL thickness in the AP + LSP sample (65 μm) is greater than that of the AP + HT + LSP sample (40 μm). The precipitates are observed near the LDL layer. This difference in SDL thickness may be attributed to variations in dislocation density between the as-printed and heat-treated samples. The combined effects of grain refinement and precipitation hardening introduced by heat treatment likely restricted dislocation movement, thereby influencing the depth of the SDL layer. As evident from Fig. 6, a highly deformed grain structure is observed in the SDL layer, where SPD has distorted the grains to such an extent that the surface appears nearly featureless even at high magnification, due to the collapse of distinct grain boundaries. This is characteristic of SPD and supports the grain refinement trends observed in EBSD analysis on peened samples. In contrast, the medium deformed layer (MDL), located just beneath the SDL, exhibits a fine columnar martensitic microstructure, indicating reduced plastic strain and partial retention of the as-solidified microstructure. This contrast between the SDL and MDL confirms the gradient nature of deformation and microstructural

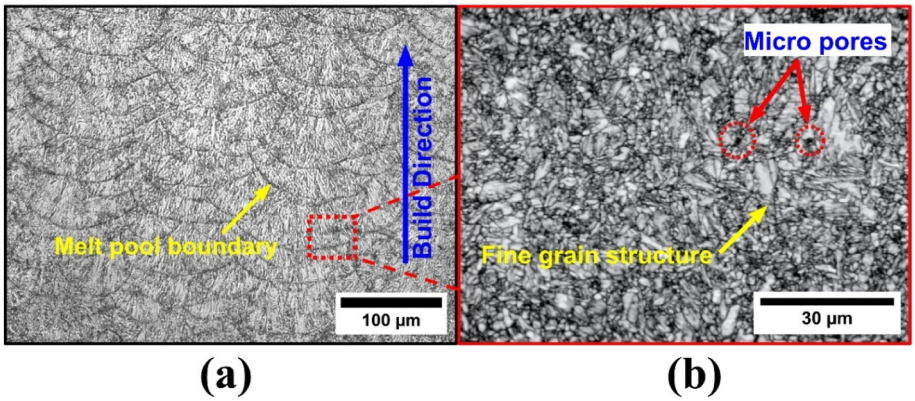


Fig. 4. The grain morphology of the AP sample showing (a) melt pool boundaries and (b) a fine martensitic microstructure. [Surface orientation is parallel to the BD].

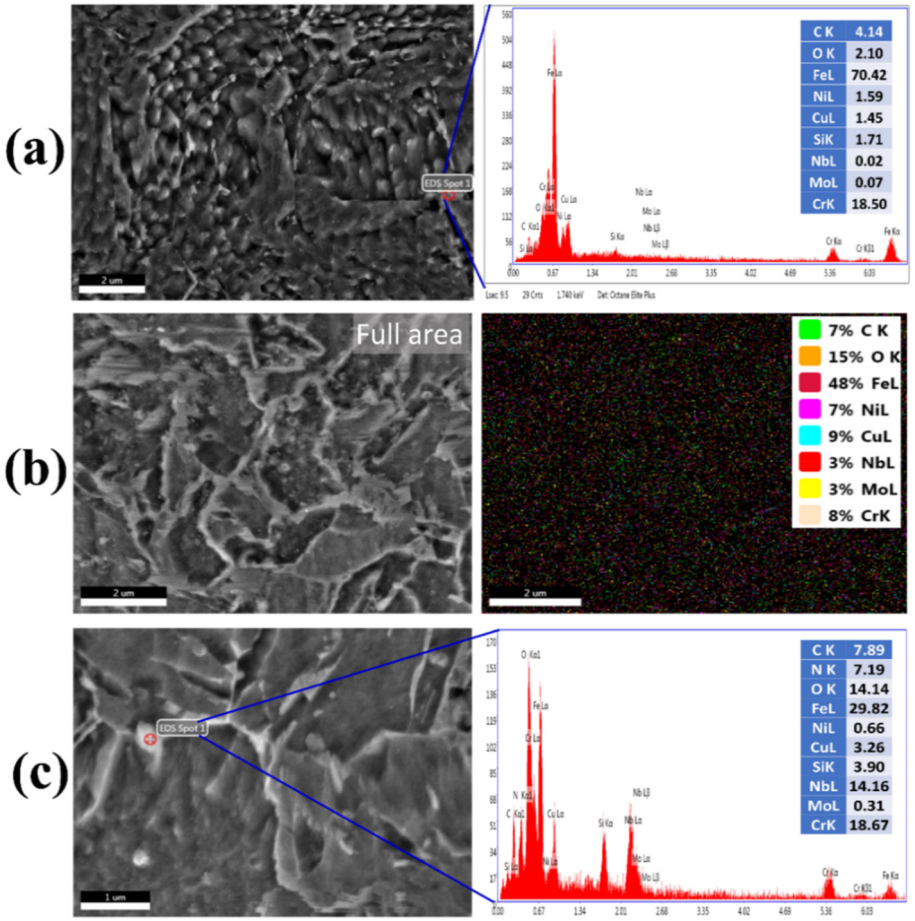


Fig. 5. The grain morphology and their respective EDS analysis of (a) the AP sample, (b) the AP + HT sample's chosen area, its consolidated elemental map, and (c) the presence of Nb-rich precipitates in the AP + HT sample with their respective spectrum. [Surface orientation is perpendicular to the BD].

evolution resulting from LSP.

As discussed by the authors in their previous work [9], the IPF map in Fig. 7(a) shows the presence of fine columnar grains with an average grain size of 7.14 µm. The phase fraction analysis shows the presence of the RA fraction (2.1 %). The high Cr/Ni ratio and the rapid solidification associated with the SLM process resulted in a higher martensitic fraction in the microstructure. Also, the grains are randomly oriented and have no preferred crystallographic texture, which indicates that the 67° rotating scanning strategy successfully mitigated the melt pool boundaries. As shown in Fig. 7(b), the AP + HT sample has a fine martensitic needle-like grain morphology, with an average grain size of 4.37 µm. The significant grain refinement compared to the as-printed sample can be attributed to the presence of precipitation-hardening elements at the grain boundaries, which impede grain growth through the Zener pinning effect. The slight increase in the retained austenite fraction after heat treatment can locally soften the material, making it more susceptible to crack initiation under severe wear conditions. This increase in RA fraction from CA-H900 heat treatment contradicts the existing literature [4], highlighting the need for further investigation in this area.

Fig. 8(a) presents the IPF map, grain size distribution, and phase

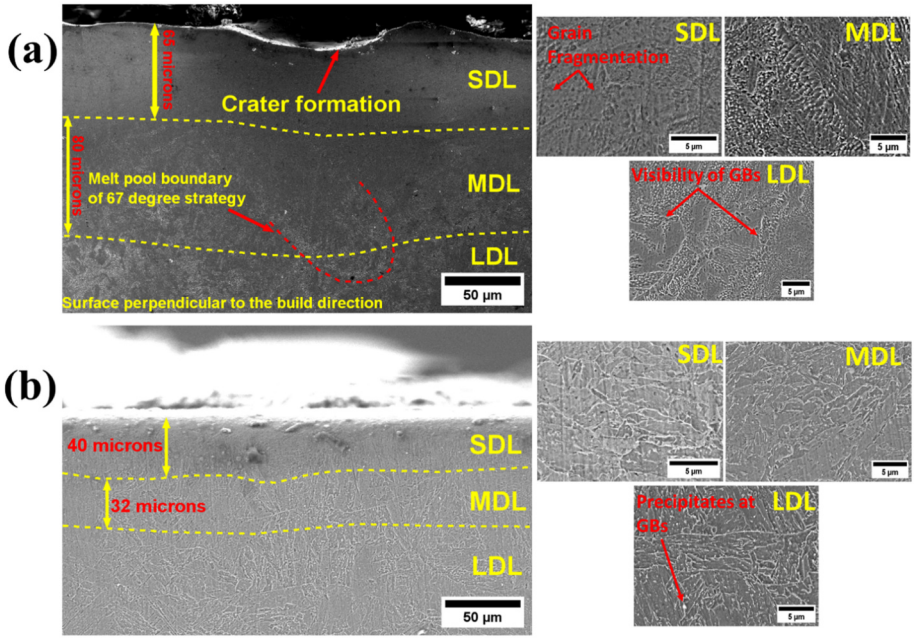


Fig. 6. Cross-sectional FE-SEM micrograph of the (a) AP + LSP sample and (b) AP + HT + LSP sample, revealing the deformed layers. [Surface orientation is perpendicular to the BD].

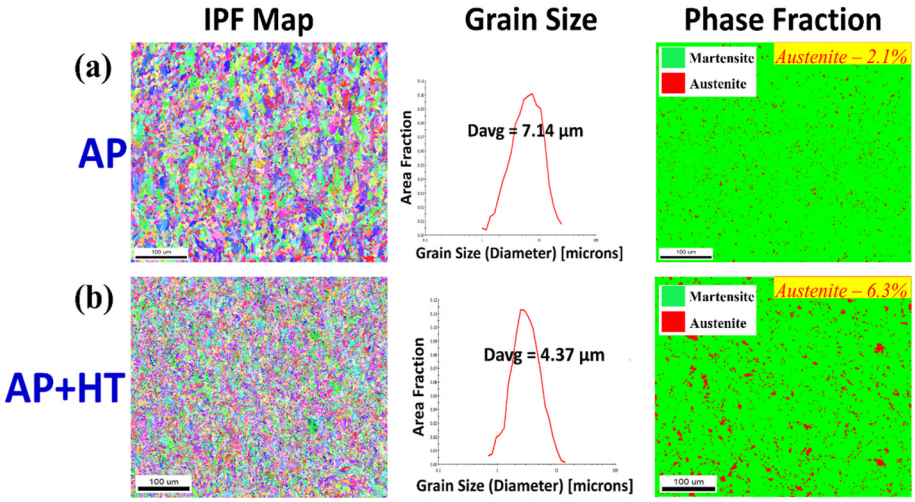


Fig. 7. The IPF map, grain size distribution and phase fraction map of the (a) AP sample, and (b) AP + HT sample, respectively [9]. [Surface orientation is parallel to the BD].

fraction of the AP + LSP sample. Grain refinement within the LSP-hardened layer arises from SPD imparted by high-strain shock waves. When the laser pulse strikes the sacrificial surface, it generates a plasma that produces a shock front travelling through the material. This shock usually induces dislocation multiplication, dynamic recovery, and sub-grain formation. Repeated pulses with 70 % overlap, given in the current study, accumulate these effects, fragmenting original grains into finer sub-micron grains. This refinement is evident in Fig. 8(a), which shows the transformation from coarser grains (7.14 µm) in the AP sample to finer grains (3.8 µm) in the AP + LSP sample. Due to this finer grain structure, a higher magnification was used for imaging the peened samples. Such grain refinement typically increases dislocation density and enhances the misorientation angles between neighbouring grains, contributing to improved hardness and wear resistance. Similarly, the AP + HT + LSP sample exhibits an even finer microstructure, with an average grain size of 3.9 µm, as shown in Fig. 8(b). The slight increase in grain size compared to AP + LSP could be attributed to the combined effects of heat treatment and peening, where heat treatment facilitates partial grain recovery while LSP continues to induce plastic deformation.

The greater grain size reduction observed in the AP sample (7.14 to 3.8 µm) compared to the AP + HT sample (4.37 to 3.9 µm) following LSP treatment is attributed to the difference in initial microstructural stability. The AP sample's more heterogeneous and residual-stress-rich structure enables extensive grain fragmentation under LSP, whereas the pre-stabilised AP + HT sample undergoes relatively limited refinement. Phase fraction analysis further reveals a significant reduction in retained austenite for both peened samples. The localized rapid cooling and intense plastic deformation induced by LSP promote a strain-induced transformation of the retained austenite, which was stabilised by heat treatment, into martensite, thereby reducing its content from 6.3 % in the AP + HT sample to 4.4 % in the AP + HT + LSP sample.

The crystallographic phases in all the samples were analysed, as depicted in Fig. 9(a). As previously reported by the authors [9],

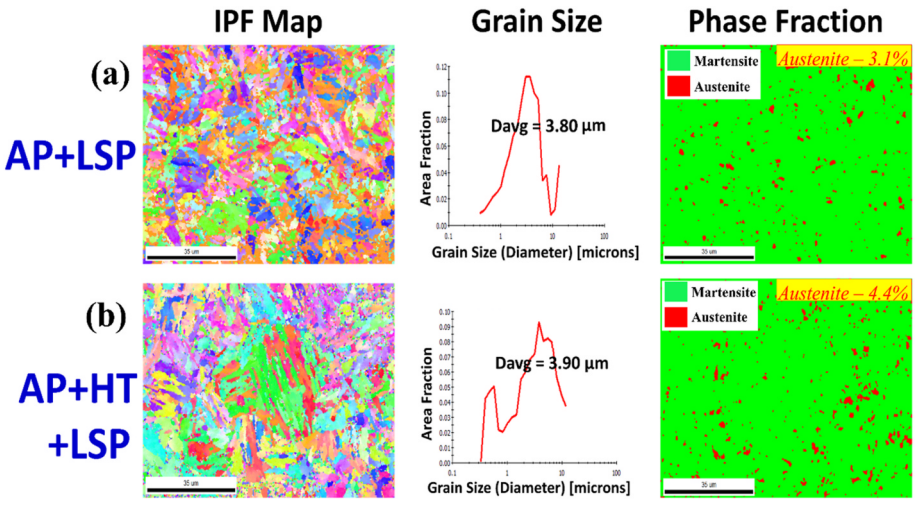


Fig. 8. The IPF map, grain size distribution and phase fraction map of the (a) AP + LSP sample, and (b) AP + HT + LSP sample, respectively [9]. [Surface orientation is parallel to the BD].

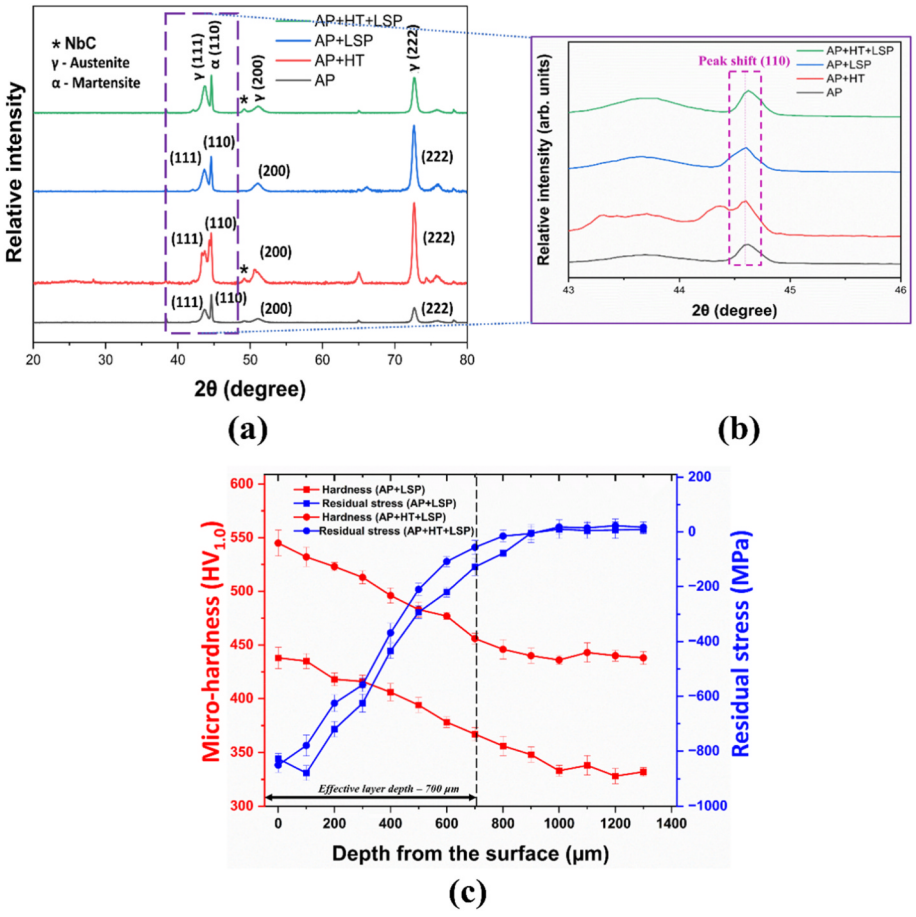


Fig. 9. (a) X-ray diffraction pattern [9], (b) high angle peak shift observed in peened samples and (c) microhardness with residual stress on surface and sub-surface depths.

martensite (BCC) (α – FeNi, ICDD PDF No. 00-37-0474) was observed to be the dominant phase across all samples [33,34]. Also, the presence of retained γ-austenite (FCC) was observed [35]. As evident from Fig. 9(b), a slight peak shift (110) toward the high-angle side in the peened samples indicates higher CRS, caused by plastic deformation from the peening process. The Bragg diffraction law explains this phenomenon of shifting peaks [36]. CRS causes decreased lattice spacing, leading to an increase in the diffraction angle (2θ), thereby shifting the diffraction peak to a higher angle side. The NbC-rich precipitates are observed in the heat-treated samples, implying successful precipitation hardening heat treatment for the as-printed 17-4 PH SS samples [21].

The microhardness and residual stress distribution from the surface to the subsurface region of the peened samples are illustrated in Fig. 9 (c). Microhardness measurements conducted at five distinct locations for

both as-peened (AP) and heat-treated (AP + HT) samples revealed average values of 330 HV and 436 HV, respectively. The average value obtained for the AP sample's CRS is −13 MPa, while the AP + HT sample exhibits a value of −6 MPa. The heat treatment process significantly refined the grain structure, facilitating precipitation hardening and Hall-Petch strengthening, thereby enhancing hardness. Following the LSP process, the hardness of the AP sample has increased to 438 HV and a CRS of −879 MPa. Similarly, the AP + HT + LSP sample exhibited a surface hardness of 545 HV and a CRS of −850 MPa at the peened surface. The mean effective layer depth of the hardened layer with CRS was measured to be approximately 700 μm for the peened samples. During LSP, SPD induced extensive dislocation generation and rearrangement, leading to grain refinement and work hardening. This process fragmented larger grains into smaller ones, introducing additional Hall-Petch strengthening and increasing dislocation density, collectively enhancing microhardness in the surface and subsurface regions [37].

The strain-hardening mechanisms activated by LSP, combined with Hall-Petch strengthening and dislocation interactions with NbC and Cu-rich precipitates, contributed to the superior microhardness observed in the AP + HT + LSP sample [38]. The LSP process generated plastic strains, resulting in higher compressive residual stresses in both surface and subsurface regions. However, as the shock waves propagated deeper into the material, their intensity lessened, leading to a gradual transition of CRS into tensile stresses beyond a depth of 800 μm [39]. The depth of CRS significantly exceeded the thickness of the SPD region. The observed increase in microhardness in the peened samples can be attributed to grain refinement, dislocation strengthening, and grain boundary strengthening mechanisms [40].

3.2. Optimization of wear parameters

The experimental investigation employed the Box-Behnken design to analyse the effects of applied load, sliding velocity, and sliding distance on the volumetric wear rate (Wv) and CoF of the AP sample. The Box-Behnken design is particularly efficient for fitting quadratic models without requiring a large set of experimental conditions, allowing for the exploration of both linear and non-linear interactions among the factors.

The 2nd order polynomial regression equation used to indicate the response surface Y for the selected input parameters is given in the following equation (5):

$$Y = b_0 + \sum_{i=1}^{k} b_i x_i + \sum_{i=1}^{k} b_{ii} x_i^2 + \sum_{i=1}^{k-1} \sum_{j=2}^{k} b_{ij} x_i x_j \quad (5)$$

Where b_{ij} = 0,1, ... …. ….k and b_0 is the arithmetic average of all outcomes.

Table 3 presents the selected factors, their units, notations, and design levels, while Table 4 displays the experimental design matrix with the corresponding responses. The objective of this experiment was to investigate the effects of these input parameters on the volumetric wear rate and the CoF of as-printed 17-4 PH SS.

The ANOVA results in Table 5 demonstrated that the applied load (A) and sliding distance (C) significantly influenced the wear rate with p-values of 0.0002 and 0.0001, respectively, both being well below the significance level of 0.05. Sliding velocity (B) also had a statistically significant effect ($p = 0.0110$), though its influence was less pronounced. The high F-values for the applied load (104.67) and sliding distance (107.52) indicate a strong effect on the wear rate. Additionally, the quadratic terms for applied load (A^2) and sliding velocity (B^2) were significant ($p = 0.0049$ and $p = 0.0063$), reflecting non-linear relationships between these factors and the wear rate. However, the interaction effects (AB, AC, BC) were statistically insignificant ($p > 0.05$), suggesting minimal combined influence of these factors on the wear rate. The high R^2 value (0.981) and adjusted R^2 (0.949) confirm that the quadratic model accurately predicts the volumetric wear rate.

Table 3
Experimental variables and levels in wear parameter.

Factors	Units	Notations	Levels		
			−1	0	+1
Applied load	N	A	40	50	60
Sliding velocity	m/s	B	1	2	3
Sliding distance	m	C	1000	2000	3000

Table 4
Experimental results for volumetric wear rate.

Std Order	Run	Applied load	Sliding distance	Sliding velocity	Wear rate	CoF
		N	M	m/s	mm^3/m	
10	1	50	3	1000	0.0302	0.665
2	2	60	1	2000	0.0315	0.619
5	3	40	2	1000	0.0233	0.604
15	4	50	2	2000	0.0334	0.619
3	5	40	3	2000	0.0263	0.624
6	6	60	2	1000	0.0324	0.648
13	7	50	2	2000	0.0347	0.613
14	8	50	2	2000	0.0338	0.601
11	9	50	1	3000	0.0341	0.625
4	10	60	3	2000	0.0333	0.678
8	11	60	2	3000	0.0383	0.652
7	12	40	2	3000	0.0314	0.585
9	13	50	1	1000	0.0248	0.615
12	14	50	3	3000	0.0369	0.652
1	15	40	1	2000	0.0249	0.629

For the CoF, the ANOVA results, as shown in Table 6, indicated that applied load and sliding velocity significantly affected friction behaviour with p-values of 0.0077 and 0.015, respectively. Their corresponding F-values (18.46 for A and 13.19 for B) emphasize their substantial impact on CoF. The B^2 was also significant ($p = 0.022$), highlighting a non-linear relationship between sliding velocity and CoF. Sliding distance and all interaction terms (AB, AC, BC) exhibited p-values greater than 0.05, indicating no significant effect on the CoF. This suggests that changes in sliding distance and interactions between factors do not alter frictional behaviour significantly enough. The model exhibited an R^2 value of 0.91 and an adjusted R^2 of 0.7512, indicating moderate model accuracy for the CoF.

For the volumetric wear rate and CoF, the coded equations (1) and (2) are given below:

$$\text{Volumetric wear rate} = 0.0339667 + 0.0037A + 0.001425B + 0.00375C + 0.0001AB + -0.00055AC + -0.00065BC + -0.00255833A^2 + -0.00240833B^2 + -5.83333e-05C^2 \quad (1a)$$

$$\text{CoF} = 0.611 + 0.019375A + 0.016375B + -0.00225C + 0.016AB + 0.00575AC + -0.00575BC + 0.00475A^2 + 0.02175B^2 + 0.0065C^2 \quad (2a)$$

The applied load was the most influential factor on both wear rate and CoF [41]. Increasing the load resulted in higher wear rates due to increased contact pressure, leading to intensified material removal. Similarly, the CoF increased with higher load due to greater asperity deformation and adhesive wear. Sliding velocity significantly impacted CoF and moderately affected wear rate. Higher velocities led to elevated surface temperatures, reducing material strength and promoting wear. However, beyond a threshold, the CoF slightly plateaued due to the possible formation of lubricious oxide layers. Sliding distance strongly influenced the wear rate but had minimal effect on CoF. Prolonged sliding increased wear due to the continuous exposure of the surface to frictional forces. However, the CoF remained stable, indicating that wear mechanisms dominated over frictional changes. interaction terms

Table 5
Evaluation of volumetric wear rate using ANOVA.

Source	Sum of squares (SS)	Degree of freedom (DoF)	Mean squares (MS)	F-value	*p*-value (Prob > F)	Status
Model	0.0003	9	0.0000	30.14	0.0008	Significant
A-load	0.0001	1	0.0001	104.67	0.0002	
B-sliding velocity	0.0000	1	0.0000	15.53	0.0110	
C-distance	0.0001	1	0.0001	107.52	0.0001	
AB	4.000E-08	1	4.000E-08	0.0382	0.8527	
AC	1.210E-06	1	1.210E-06	1.16	0.3313	
BC	1.690E-06	1	1.690E-06	1.62	0.2597	
A^2	0.0000	1	0.0000	23.10	0.0049	
B^2	0.0000	1	0.0000	20.47	0.0063	
C^2	1.256E-08	1	1.256E-08	0.0120	0.9170	
Residual	5.232E-06	5	1.046E-06			
Lack of fit	4.345E-06	3	1.448E-06	3.27	0.2431	Not significant
Pure error	8.867E-07	2	4.433E-07			
Cor Total	0.0003	14	0.0000			
R^2	0.9819					
Adj R^2	0.9493					

Table 6
Evaluation of CoF using ANOVA.

Source	Sum of squares (SS)	Degree of freedom (DoF)	Mean squares (MS)	F-value	*p*-value (Prob > F)	Status
Model	0.0083	9	0.0009	5.70	0.0349	Significant
A-load	0.0030	1	0.0030	18.46	0.0077	
B-sliding velocity	0.0021	1	0.0021	13.19	0.0150	
C-distance	0.0000	1	0.0000	0.2490	0.6390	
AB	0.0010	1	0.0010	6.30	0.0539	
AC	0.0001	1	0.0001	0.8131	0.4085	
BC	0.0001	1	0.0001	0.8131	0.4085	
A^2	0.0001	1	0.0001	0.5122	0.5062	
B^2	0.0017	1	0.0017	10.74	0.0220	
C^2	0.0002	1	0.0002	0.9591	0.3724	
Residual	0.0008	5	0.0002			
Lack of fit	0.0006	3	0.0002	2.56	0.2933	Not significant
Pure error	0.0002	2	0.0001			
Cor Total	0.0092	14				
R^2	0.9111					
Adj R^2	0.7512					

between parameters (AB, AC, BC) were statistically insignificant for both wear rate and CoF, suggesting that the effects of load, velocity, and distance operate independently rather than synergistically.

Fig. 10(a) presents the 3D surface plot illustrating the effect of load and sliding velocity on wear rate, with the sliding distance fixed at 2000 m. The wear rate exhibits a quadratic increase with both parameters, with load having a more pronounced influence compared to sliding velocity. It can be seen that a small dip in wear rate at a high load and high-velocity combination might be due to material melting and subsequent adherence on the interaction surface, leading to low-volume loss. Fig. 10(b) depicts the 3D surface plot showing the impact of load and sliding distance on wear rate, with sliding velocity maintained at 2 m/s. A quadratic increase in wear rate is observed as both parameters rise, with load exerting a stronger effect than sliding distance. Fig. 10(c) illustrates the 3D surface plot for sliding velocity and sliding distance, with the load set at 50 N. The results reveal a nonlinear interaction, where the wear rate increases with both parameters. The minimum wear rate occurs at the lowest sliding velocity and sliding distance, while the maximum wear rate is observed at the highest parameter values. The accuracy of the developed RSM model was further validated using a predicted vs. actual plot, as depicted in Fig. 10(d), where the data points closely follow the regression line, indicating a high degree of correlation between predicted and actual values.

Fig. 11(a–c) presents the 3D surface plots illustrating the combined influence of load, sliding velocity, and sliding distance on the CoF. The CoF exhibits a complex relationship with these selected parameters, with sliding velocity having a slightly greater effect than load and sliding distance. At lower loads, CoF remains stable, while at higher loads, increasing velocity results in a slight reduction in CoF due to reduced adhesion. Similarly, CoF decreases slightly with increasing sliding distance at higher loads, likely due to oxide film formation. Higher sliding velocities and sliding distances further promote tribo-layer formation, stabilizing CoF. The predicted vs. actual plot, as shown in Fig. 11(d), confirms the model's reliability as having a good fit between actual and predicted values.

3.3. Validation study

To ensure a comprehensive evaluation of the wear performance of additively manufactured 17-4 PH SS, the wear test conditions were carefully designed to utilize the hardened layer depth achieved via LSP fully. The hardened layer depth for the LSP-treated samples was found to be approximately 0.7 mm. It was essential to design the wear test to engage this depth effectively. To achieve this, the theoretical volume of the cylindrical pin (10 mm in diameter and 30 mm in height) was calculated as 2356.19 mm^3, based on the pin geometry. The target post-test pin volume was set at 2300 mm^3, corresponding to a final pin height of 29.3 mm, representing a volume loss of 56.19 mm^3. This target volume loss was selected to ensure that the wear depth would penetrate the hardened layer, enabling a comprehensive assessment of its effectiveness. The target wear rate of 0.28 mm^3/m was calculated based on a mid-range sliding distance of 2000 m to achieve the desired volume loss (56.19 mm^3). Using RSM, a target wear rate of 0.28 mm^3/m with minimum CoF condition was established to identify the optimal solution with high desirability (>0.95 %) that would result in the desired wear rate. The optimal wear parameter combination of load = 40 N, sliding

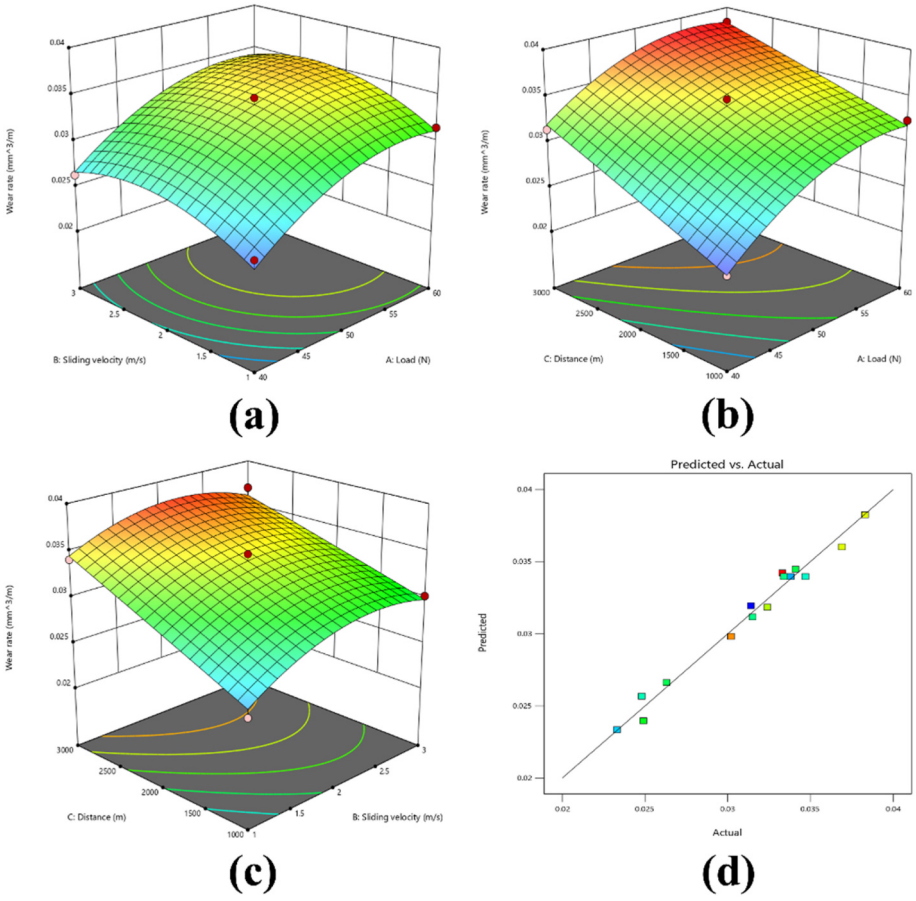


Fig. 10. 3D surface plot for wear rate (a) Applied load vs sliding velocity, (b) Applied load vs sliding distance, (c) Sliding velocity vs sliding distance, and (d) Interaction of actual vs predicted values.

velocity = 1.95 m/s, and sliding distance = 2084 m was predicted.

As shown in Table 7, a validation study was conducted, and an actual wear rate of 0.0284 mm^3/m with a corresponding volume loss of 56.8 mm^3 and CoF of 0.655 was observed with less than 10 % error with the predicted value. The quadratic model derived from the Box-Behnken design reasonably predicted the experimental outcomes, confirming the model's suitability for wear performance analysis.

3.4. High-temperature wear behaviour

The optimized process parameters serve as a performance-limiting condition for evaluating the wear resistance of the hardened layer at both room and elevated temperatures. Also, this experimental design ensures that the wear tests are not only representative of realistic wear conditions but also sufficiently challenging to test the limits of the hardened layer's performance. The selected wear test conditions are shown in Table 8.

The wear behaviour of AP samples subjected to HT and LSP were analysed at room temperature at 25 °C and elevated temperatures (150, 250, and 350 °C), with wear rate results shown in Fig. 12. Elevated temperatures caused thermal softening and led to an increased wear rate for all samples. Higher temperatures increased contact area and tangential stresses, raised friction and thereby resulted in increased wear rate [42].

The wear depth as a function of sliding distance highlights the effects of processing conditions and temperature on material wear resistance for all samples, as shown in Fig. 13(a–d). The as-printed (AP) sample exhibits a progressive increase in wear with sliding distance, with higher wear at elevated temperatures due to thermal softening. The wear rate for the AP + HT sample at room temperature is 0.0415 mm^3/m, which is notably higher than that of all samples. The precipitation-hardened sample (AP + HT) shows the highest wear across all distances, attributed to its brittle morphology and oxidation wear, further exacerbated by a higher retained austenite fraction (6.3 %). The AP sample exhibits lower wear rates than heat-treated samples. The laser shock peened sample (AP + LSP) exhibits the lowest wear across all conditions, benefiting from subsurface hardening, which enhances resistance to material loss. The combined AP + HT + LSP sample shows relatively moderate wear but experiences a sharp increase at 350 °C during the initial sliding distance, as evident in Fig. 13(d), suggesting possible combined thermal effects (high temperature and friction-induced temperature) on the hardened layer. The slope of the wear rate curve displays an upward trend with increasing temperatures. Overall, heat treatment increases wear due to the loss of strength gained by retained austenite fraction and oxidation, while laser shock peening significantly reduces wear, with AP + LSP providing the most consistent wear resistance across all sample and temperature conditions.

The CoF trend across all four conditions showed distinct variations influenced by the processing conditions and temperature effects, as shown in Fig. 14(a–d). For the AP sample, the CoF starts high during the running-in period (R.P) and stabilizes in the steady-state period (S.S.P). At room temperature, the CoF remains relatively higher compared to elevated temperatures. At 350 °C, a notable reduction in CoF was observed due to oxide layer formation, which reduces adhesion and friction. As for the AP + HT sample, the overall CoF for elevated temperature conditions (150 °C and 250 °C) was slightly lower than in the RT condition. The severe abrasion and delamination wear mechanisms were more pronounced at high-temperature (350 °C) condition. The brittle morphology of the heat-treated sample affected the surface stability and gradually increased the CoF at S.S.P. LSP-treated samples

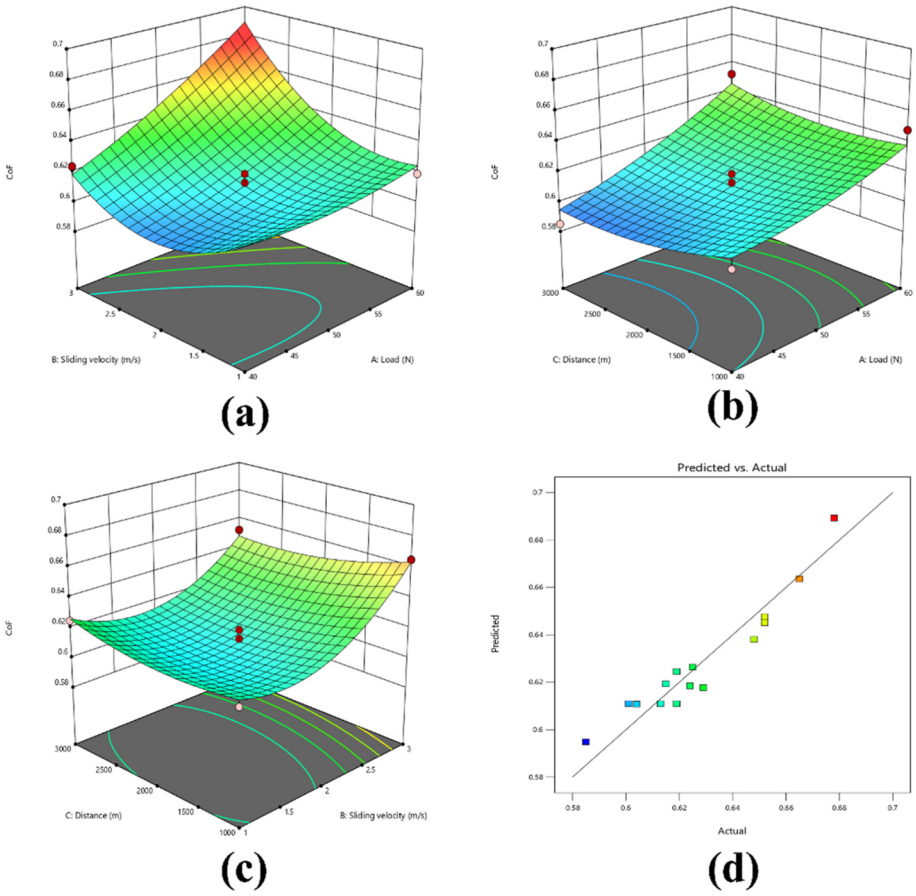


Fig. 11. 3D surface plot for COF (a) Applied load vs sliding velocity, (b) Applied load vs sliding distance, (c) Sliding velocity vs sliding distance, and (d) Interaction of actual vs predicted values.

Table 7
Validation study.

Responses	Predicted values	Desirability	Experimental values	Difference	Error (%)
Wear rate (mm^3/m)	0.028	1.95	0.0284	0.0004	1.43
CoF	0.596		0.655	0.059	9.89

Table 8
The selected wear test parameters for the high-temperature wear study.

Parameter	Value
Load	40 N
Sliding velocity	1.95 m/s
Sliding distance	2084 m
Operating temperatures	Room temperature, 150 °C, 250 °C, and 350 °C

exhibit a generally higher CoF in S.S.P compared to the AP and AP + HT conditions. The increased surface roughness and work-hardening effects from LSP contributed to higher friction initially. However, at elevated temperatures, the CoF stabilizes, suggesting that LSP enhances wear resistance while still benefiting from oxide formation. At 150 °C and 350 °C temperature conditions on the AP + HT + LSP sample, the oxide layer that formed on the wear track fractured during initial R.P., leading to an uneven CoF pattern in S.S.P, as observed in Fig. 14(d). The lowest CoF is observed at higher temperatures, likely due to the combined benefits of HT-induced precipitation hardening and LSP-induced strain hardening.

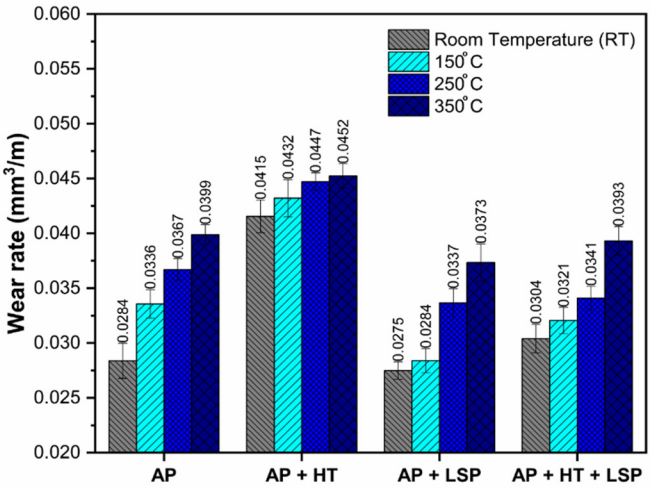


Fig. 12. Comparison of the sample's wear rate at room and elevated temperature conditions.

Fig. 15(a–p) presents SEM micrographs of the worn-out surfaces of the AP, AP + HT, AP + LSP, and AP + HT + LSP samples, while Table 9 and Fig. 16(a–d) provides the corresponding EDS spectra of the worn tracks. The results indicate that the intensity of the oxide layer increases with rising wear temperature. The combined effects of sliding friction and a high-temperature environment elevated the contact temperature, promoting oxidative wear. This leads to the formation and subsequent

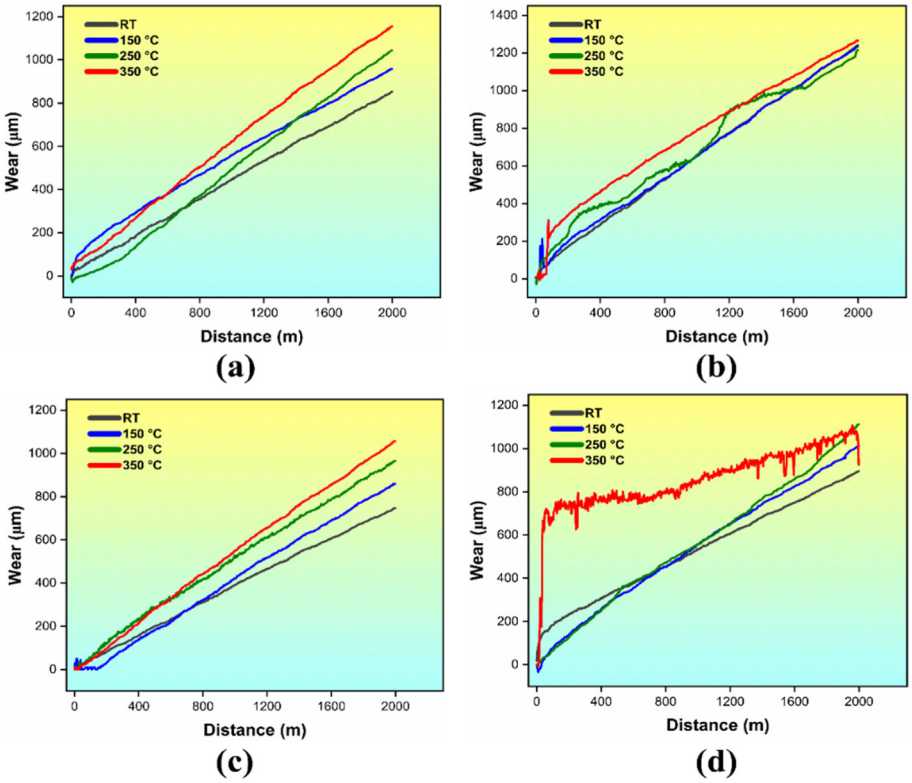


Fig. 13. Plot showing the wear observed with respect to sliding distance for (a) AP, (b) AP + HT, (c) AP + LSP, and (d) AP + HT + LSP samples.

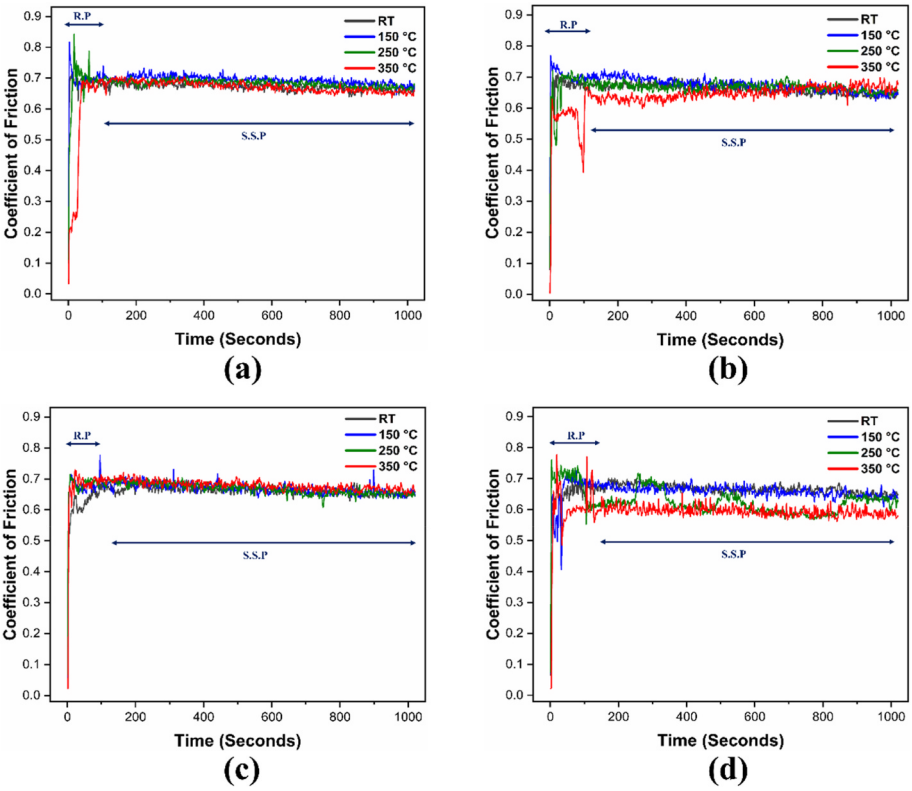


Fig. 14. Evolution of COF against sliding time for (a) AP, (b) AP + HT, (c) AP + LSP, and (d) AP + HT + LSP samples.

oxidation of wear debris across all four samples. The wear rate of the AP sample increases with an increase in operating temperature and exhibits mild cracks along the wear track, while at elevated temperature, severe delamination becomes more pronounced, as evident from Fig. 15(b–d). Contrary to the existing literature [21], the AP + HT sample, despite its increased hardness, shows a significantly higher volume loss compared

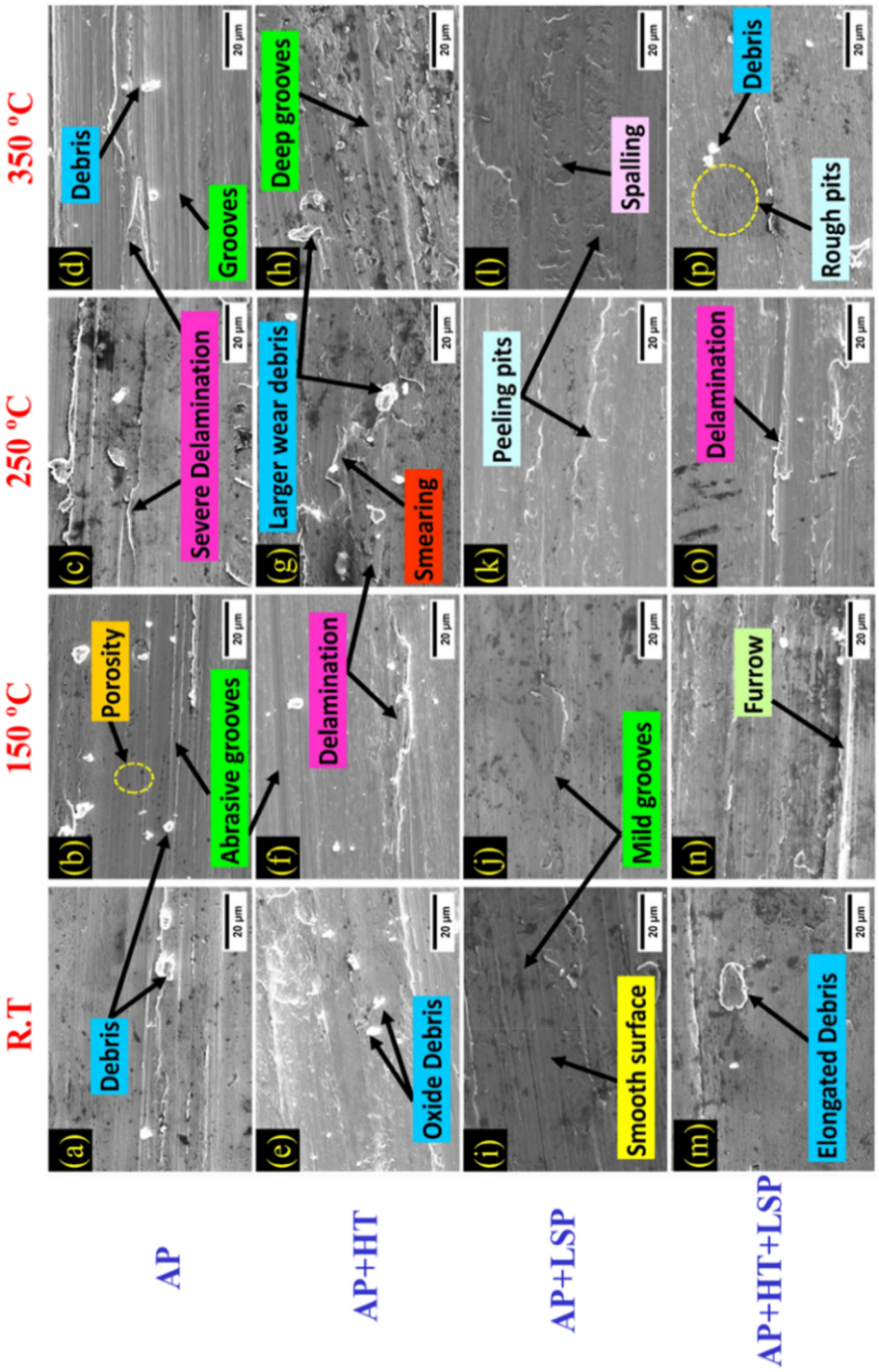


Fig. 15. (a–p) Worn surface morphology of all samples at room and elevated temperatures.

Table 9
EDS analysis of the region, as shown in Fig. 14(a–p) (at. %).

Region	O	C	Cr	Cu	Fe	Region	O	C	Cr	Cu	Fe
Spot a	1.8	3.6	14.5	3.7	65.8	**Spot i**	2.4	1.3	14.4	3.7	66
Spot b	6.3	12.7	12.7	3.3	59.1	**Spot j**	2.8	5.2	14.1	3.5	64.1
Spot c	15.3	42.3	3.2	0.5	16.2	**Spot k**	10.7	9.7	12.8	3.3	58.2
Spot d	14.5	10.3	11.9	3.2	55.2	**Spot l**	13.7	8.2	12.4	3.2	57.1
Spot e	37.5	5.8	2.4	0.5	51.6	**Spot m**	4.3	2.5	15.1	3.8	68.4
Spot f	37.3	23.6	3.1	1.2	31.1	**Spot n**	10.7	7.3	13.2	3.4	59.9
Spot g	23.5	5.5	14.1	2.5	49.9	**Spot o**	13.3	14.4	11.4	3	52.3
Spot h	43.7	9.5	7.1	0.1	38.8	**Spot p**	46.5	23.4	2.2	0.1	23.1

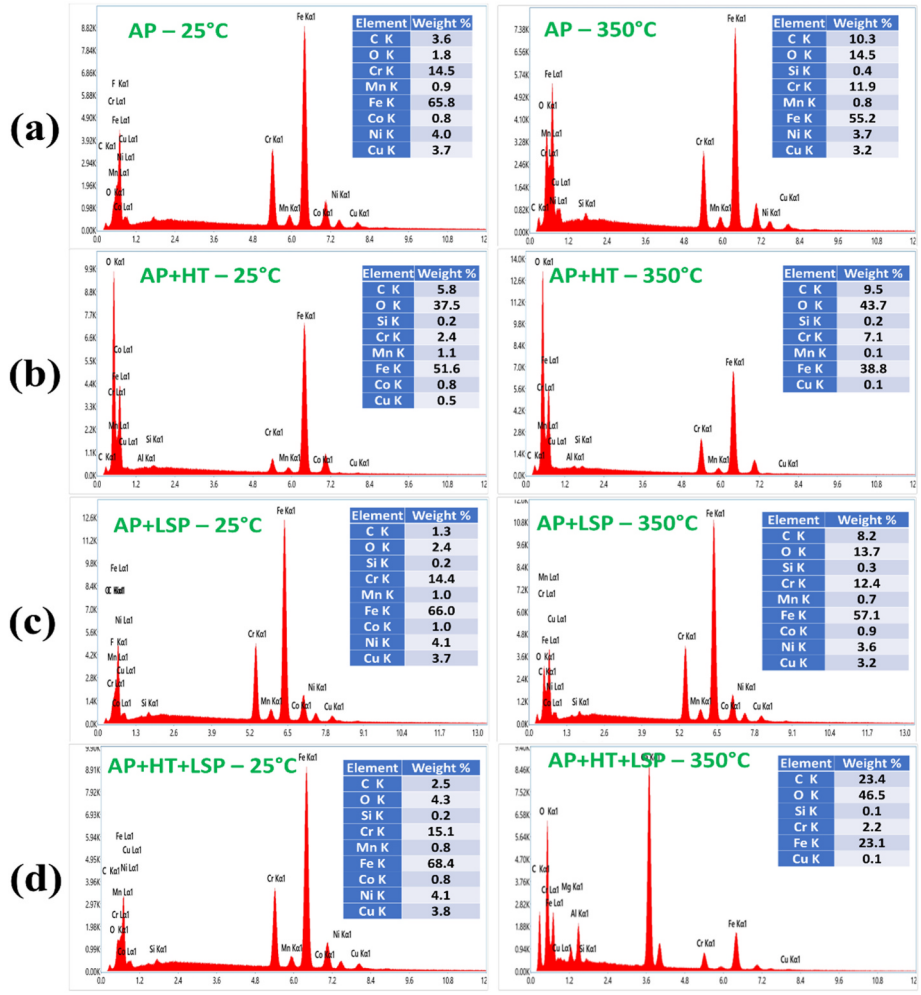


Fig. 16. EDS analysis of the worn-out surface of (a) AP, (b) AP + HT, (c) AP + LSP, and (d) AP + HT + LSP samples tested under room and elevated temperature conditions, respectively.

to the AP sample across all temperature conditions. After precipitation hardening, the material becomes harder and brittle, showing significant wear debris in its worn surface morphology, as shown in Fig. 15(e–h).

At high temperatures, deeper grooves and severe abrasive wear become more pronounced due to the three-body wear mechanism, where trapped abrasive particles between the sliding surfaces cause additional wear. This brittleness leads to non-uniform adhesion of the worn layers, resulting in cracks and a higher wear rate compared to the ductile morphology of the AP sample. Under high load conditions, these oxide layers can detach, and continued sliding contact leads to their fragmentation, generating abrasive oxidized particles. This process increases friction and accelerates wear rates. This observation aligns with the existing literature [43]. The higher retained austenite fraction in the AP + HT sample also contributes to premature sliding wear due to its softer nature. Fig. 16(b) shows a higher level of oxygen content in the worn-out surface in the AP + HT sample at both RT and 350 °C temperature conditions. At elevated conditions, the oxide layer on the wear track fractures, further accelerating wear and volume loss on the heat-treated samples. Increased contact stress and temperature cause significant oxidation in the wear tracks, where the oxide plateaux seen at room temperature (Fig. 15(e)) deteriorate under elevated temperatures, producing oxide wear debris that further damages the softer interface through abrasive wear. Additionally, the delamination of the iron oxide film contributes to reduced wear resistance in the AP + HT sample.

At elevated temperatures, it is well understood that recovery processes and increased dislocation mobility can reduce the strengthening effects imparted by severe plastic deformation by LSP. However, in the present study, the AP + LSP continues to demonstrate improved friction and wear resistance compared to the untreated AP condition, even under such thermal exposure. This behaviour can be attributed to the synergistic effect of microstructural stability and mechanical stress retention within the LSP-hardened surface layer. The propagation of high-strain shock waves during LSP not only induces SPD but also introduces rapid localised thermal cycling and grain fragmentation, which likely facilitates the formation of fine Cu-rich precipitates near the surface in 17-4 PH stainless steel. These precipitates, along with existing Nb-rich carbides, act to pin grain boundaries and hinder grain coarsening, thereby enhancing the thermal stability of the refined microstructure and delaying dislocation recovery. These microstructural changes contribute to Hall-Petch strengthening and increase surface hardness. Although elevated temperatures can partially relax residual stresses, the CRS introduced by LSP up to −800 MPa is not entirely relieved even at 350 °C. This retained CRS plays a significant role in suppressing crack initiation and propagation under sliding contact, contributing to mechanical integrity. Thus, despite the potential for softening at elevated temperatures, the combined effects of precipitate-stabilised grain boundary pinning and retained CRS help preserve surface hardness and structural refinement. These mechanisms collectively explain the superior wear resistance observed in the AP + LSP and AP + HT + LSP samples at high temperatures.

Fig. 17 depicts the SEM and XRD analysis of the worn debris from the AP + HT sample processed at 350 °C. The worn debris was primarily in

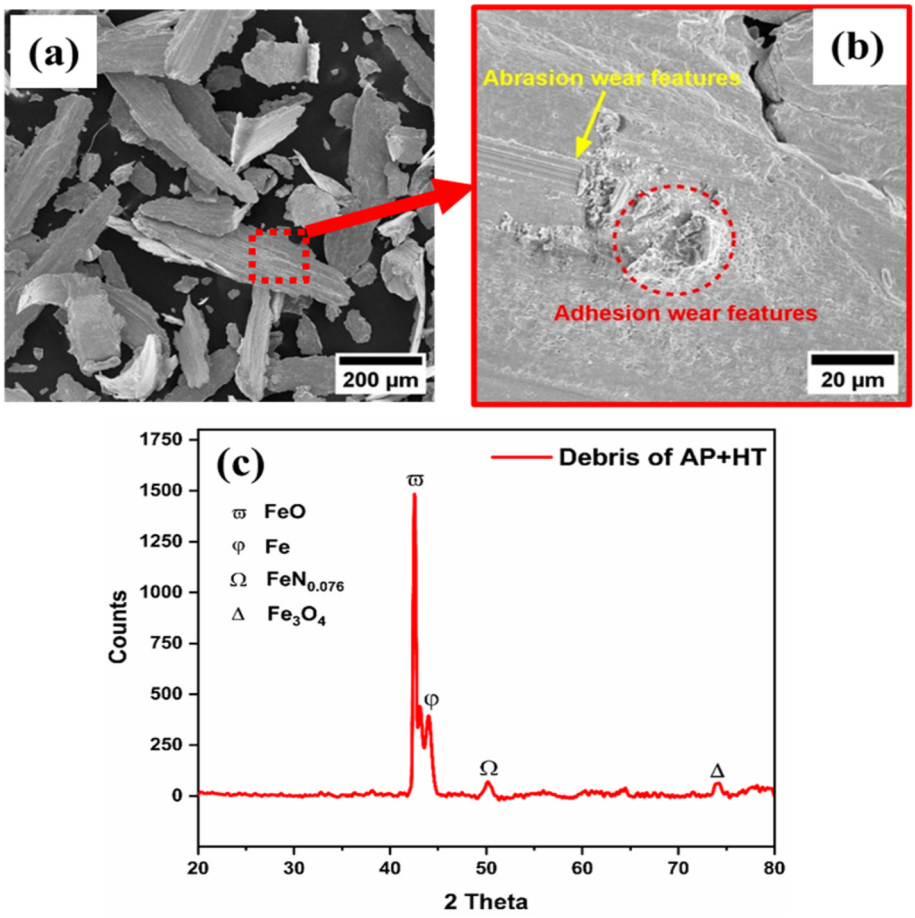


Fig. 17. SEM analysis on AP + HT sample showing (a) worn-out debris in the form of flakes, (b) prominent wear mechanisms at play, and (c) XRD pattern for 350 °C.

the form of flakes, as shown in Fig. 17(a). The prominent wear mechanisms identified were delamination, adhesion, and abrasion, with both adhesion and abrasion features visible on the worn debris in Fig. 17(b). XRD analysis confirmed the presence of iron oxides, such as FeO and Fe_3O_4, on the worn surface of the AP + HT sample, indicating oxidation wear, as evident from Fig. 17(c). This is in accordance with the existing literature [21]. The EDS maps in Fig. 16 serve as qualitative indicators, with all spectra acquired under identical detector settings and consistent sample orientation to minimize topography-related artefacts. Regions exhibiting prominent oxide nodules in wear tracks show correspondingly elevated oxygen counts, confirming the occurrence of oxidation wear. Specifically, higher oxygen and carbon signals observed in the high-temperature wear tracks are interpreted as evidence of oxide layer formation and carbon-rich debris transfer from the counter surface. More importantly, these EDS trends correlate well with wear morphological observations, which reveal the presence of oxide plateaux and loose debris in Fig. 15(e), as well as with the XRD result in Fig. 17(c), which confirm the formation of iron oxide phases. Fig. 18 illustrates the wear mechanism involved in all the sample conditions.

At elevated temperatures, oxidative wear becomes the dominant wear mechanism due to accelerated oxidation rates, which promote the formation of oxide layers on the worn surface. The heat treatment

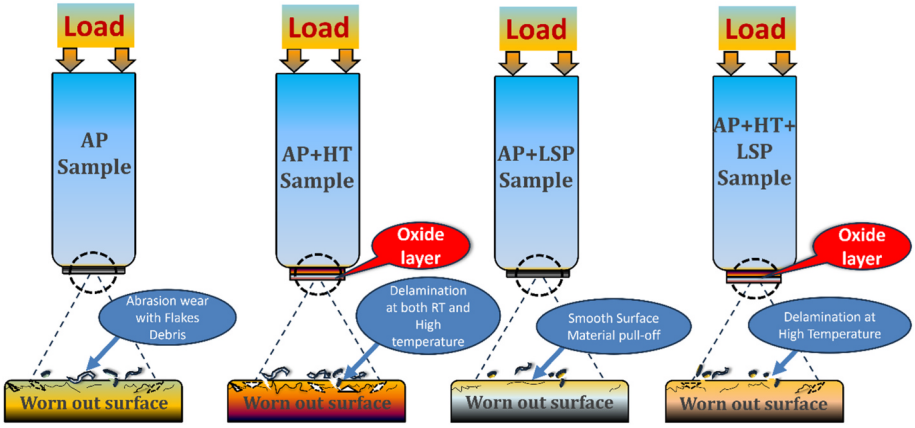


Fig. 18. Illustration of the dry sliding wear mechanism of all the samples.

process led to the formation of phases more susceptible to oxidation and delamination, while the brittleness from precipitation hardening facilitated crack initiation and propagation, allowing oxygen to penetrate and enhance oxidation wear, thus increasing its wear rate. The AP + HT sample exhibited increased hardness due to precipitation hardening, yet this led to a higher wear rate, which deviates from the expected behaviour predicted by Archard's law. This suggests that while hardness is a crucial factor, brittleness and microstructural characteristics also significantly influence wear behaviour. When metals slide against each other, wear tends to be more pronounced due to higher friction at the contact interface. In contrast, surfaces covered by an oxide layer typically experience a lower wear rate, but this is only valid if the oxide layer has lubricating properties [44]. In this case, the oxide layer consists of iron oxide particles, leading to intense abrasion and three-body wear between the contact surfaces. This interaction results in deeper grooves in the unpeened samples as temperature increases, along with severe delamination, which further accelerates wear volume loss, as evident from Fig. 15(h). In this study, the formation of oxide layers with elevated oxygen content on the heat-treated 17-4 PH SS sample under high-temperature conditions was confirmed using EDS line scans (Fig. 16 (b&d)) and XRD analysis (Fig. 17(c)), validating the role of oxidation in intensified wear behaviour.

As for the peened samples, a significant reduction in wear rate is observed for both room and high-temperature conditions. Uniform flattering of wear track is observed for all temperature conditions on both AP + LSP and AP + HT + LSP samples, leading to a lower wear rate, as shown in Fig. 15(i–p). It is observed that abrasive wear is significant at room temperature due to high Ra values [45], while oxidation and delamination wear become more prominent at higher temperatures. As the test temperature rises, the size of the wear debris also increases, and this change in size and shape is due to the severe delamination wear observed at elevated temperatures. However, after LSP treatment, the severity of delaminated and abrasive wear significantly decreases.

The application of LSP to as-printed 17-4 PH SS samples resulted in a significant improvement in wear resistance. The AP + LSP samples demonstrated a lower wear rate compared to AP samples across all temperature conditions. For instance, at room temperature, the wear rate of the AP + LSP sample was 0.0275 mm^3/m, which was lower than the 0.0284 mm^3/m observed for the AP sample. This trend continued at elevated temperatures, with the AP + LSP sample consistently showing lower wear rates. With increasing temperature, the extent of plastic deformation and material spalling also increases, leading to a slightly rougher worn surface and a higher wear rate in unpeened samples, as evident from Fig. 15(d&h). However, after LSP treatment, the wear mechanism transitions from severe adhesive and abrasive wear with notable delamination to a milder combination of abrasive and adhesive wear [46]. LSP treatment mitigates the severe wear mechanisms by inducing CRS and work hardening in the material.

CRS introduced by LSP fundamentally modifies the stress state at the sliding surface. Under tribological loading, the presence of TRS at asperities promotes crack initiation and propagation. In contrast, a CRS field opposes tensile opening, delaying crack nucleation and suppressing microcrack growth. This leads to reduced material removal and improved resistance to severe wear mechanisms. In this study, the AP + LSP sample demonstrated a 3 % reduction in wear rate at room temperature and a 6.5 % reduction at 350 °C compared to the AP condition. Residual stress measurements revealed that the AP sample had a CRS of −13 MPa and the AP + HT sample had −6 MPa. After LSP, both samples exhibited a substantial increase in CRS to approximately −800 MPa. Additionally, nearly a 25 % increase in surface hardness was observed after the peening process for both samples, further contributing to enhanced tribological performance. These improvements are attributed to the beneficial effects of CRS in mitigating surface damage mechanisms such as adhesive, delamination, and fatigue spallation.

The increase in CRS and hardness resulted in a lower wear rate on peened samples by uniformly flattening the wear track at all temperature conditions, thereby reducing the severity of delamination and abrasive wear. The presence of refined grains due to LSP also contributed to this improvement, as finer grains could better accommodate plastic deformation and reduce the likelihood of crack formation. The introduction of LSP treatment to heat-treated samples resulted in a substantial reduction in wear rate. At room temperature, the wear rate for AP + HT + LSP samples was 0.0304 mm^3/m, significantly lower than the 0.0415 mm^3/m for the AP + HT sample. While the wear rate for AP + HT + LSP samples across all temperature conditions was still higher than that for AP + LSP samples, the improvement was significant compared to that of other samples. This resulted in more uniform adhesion of the worn layers and reduced the severity of abrasive and delamination wear mechanisms. Additionally, the fine-grain structure and increased hardness due to precipitation hardening elements like Cu-rich precipitates and LSP contributed to enhanced wear resistance. The AP + HT + LSP samples demonstrate better wear resistance over AP and AP + HT samples due to the combined influence of precipitation-hardening elements and strain hardening. However, it is still inferior to AP + LSP samples due to the negative influence of oxidation wear and brittle morphology induced by heat treatment. The as-printed sample benefited more from the grain refinement and stress redistribution induced by the LSP process than from heat treatment.

The observed wear resistance trend (AP + LSP > AP + HT + LSP > AP > AP + HT) can be attributed to the interplay between processing techniques and material properties. From the above observations and evidence, the AP + LSP samples exhibited the highest wear resistance, primarily due to the LSP process, which introduced CRS and refined the microstructure. This enhancement enabled the material to accommodate plastic deformation better, thereby reducing the likelihood of crack formation and significantly improving wear performance. The AP + HT + LSP samples also demonstrated superior wear resistance compared to both the AP and AP + HT samples, benefiting from the combined effects of precipitation hardening and LSP treatment. While heat treatment increased hardness through the formation of strengthening precipitates, LSP mitigated the brittleness associated with this process, resulting in improved adhesion of worn layers and lower wear rates.

4. Conclusion

The study investigated the effects of heat treatment and laser shock peening on the microstructure and high-temperature wear behaviour of 17-4 PH SS. The key findings are as follows.

1. The roughness values for AP and AP + HT samples increased by 4 × and 2 × respectively after LSP, but the overlapping strategy and localized remelting effectively minimized excessive roughness and prevented microcrack formation.
2. Severe plastic deformation caused grain refinement and strain hardening, leading to increased hardness and microstructural changes extending 600–800 μm deeper into the treated layer.
3. From the RSM analysis, it is proved that the applied load and sliding distance are the dominant factors affecting the wear rate, while the applied load and sliding velocity influence the CoF.
4. The AP + LSP sample showed a slightly higher wear rate than the AP sample at room temperature due to increased surface roughness resulting from the peening process. However, at elevated temperatures, AP + LSP demonstrated superior wear resistance compared to all other samples.
5. When compared to the AP + HT sample's brittle morphology, the AP + LSP sample showed improved wear resistance by approximately 52 % at RT and 20 % at 350 °C, highlighting the effectiveness of LSP in enhancing high-temperature wear performance.
6. At elevated temperatures, the dominant wear mechanism shifts to severe delamination, wherein oxidized wear particles become trapped between the tribological surfaces, acting as a third-body abrasive layer and leading to an increased wear rate.

7. The main wear mechanisms of 17-4 PH SS samples include delamination, abrasive and oxidation wear. However, after LSP treatment, the severity of delaminated and abrasive wear significantly decreased, leading to improved wear resistance.
8. The improved tribological properties of the peened samples are attributed to work hardening, beneficial CRS, and refined grain structure, all of which effectively delay crack initiation and propagation during the wear process.
9. LSP proves to be an effective surface modification technique that mitigates the decremental effects of heat treatment while significantly improving wear resistance, particularly under elevated temperature conditions. Based on this study, for enhanced mechanical properties, combining heat treatment and LSP is advisable. For applications needing improved wear resistance, applying LSP directly to the as-printed 17-4 PH SS sample is recommended.

CRediT authorship contribution statement

S. Pradeep Kumar: Writing – review & editing, Writing – original draft, Validation, Methodology, Investigation, Conceptualization. **N. Radhika:** Writing – review & editing, Supervision. **P. Dinesh Babu:** Review, Supervision. **T. Ram Prabhu:** Conceptualization. **Jaiprakash Gautam:** Software, Resources. **V. Chakkravarthy:** Resources.

Funding

This research did not receive any specific grant from funding agencies in the public, commercial, or not-for-profit sectors.

Declaration of competing interest

The authors declare that they have no known competing financial interests or personal relationships that could have appeared to influence the work reported in this paper.

References

[1] Wu J, Ding W, Zhai Y, Qiao H, Zhao J, Mao Z, et al. Laser shock processing on selective laser melted 15-5PH stainless steel: improving mechanical properties and wear resistance. Wear 2023;522:204836. https://doi.org/10.1016/j.wear.2023.204836.
[2] Bhavar V, Kattire P, Patil V, Khot S, Gujar K, Singh R. A review on powder bed fusion technology of metal additive manufacturing. Addit Manuf Handb Prod Dev Def Ind 2017:251–61. https://doi.org/10.1201/9781315119106.
[3] Li H, Ramezani M, Li M, Ma C, Wang J. Effect of process parameters on tribological performance of 316L stainless steel parts fabricated by selective laser melting. Manuf Lett 2018;16:36–9. https://doi.org/10.1016/j.mfglet.2018.04.003.
[4] Sathyanath A, Meena A. Microstructural evolution and strain hardening behavior of heat-treated 17-4 PH stainless steel. Mater Today Commun 2020;25:101416. https://doi.org/10.1016/j.mtcomm.2020.101416.
[5] Irrinki H, Nath SD, Alhofors M, Stitzel J, Gulsoy O, Atre SV. Microstructures, properties, and applications of laser sintered 17-4PH stainless steel. J Am Ceram Soc 2019;102:5679–90. https://doi.org/10.1111/jace.16372.
[6] Garcia-Cabezon C, Hernández CG, Castro-Sastre MA, Fernandez-Abia AI, Rodriguez-Mendez ML, Martin-Pedrosa F. Heat treatments of 17-4 PH SS processed by SLM to improve its strength and biocompatibility in biomedical applications. J Mater Res Technol 2023;26:3524–43. https://doi.org/10.1016/j.jmrt.2023.08.104.
[7] Murr LE, Martinez E, Hernandez J, Collins S, Amato KN, Gaytan SM, et al. Microstructures and properties of 17-4 PH stainless steel fabricated by selective laser melting. J Mater Res Technol 2012;1:167–77. https://doi.org/10.1016/S2238-7854(12)70029-7.
[8] Kumar SP, Babu PD. Effect of laser energy density on surface morphology, microstructure and mechanical behaviour of direct metal laser melted 17-4 PH stainless steel. Int J Mater Res 2023;114:911–24. https://doi.org/10.1515/ijmr-2022-0242.
[9] S PK, P DB, Gautam J, Rai AK, Paul CP. Synergistic integration of laser shock peening and heat treatment for refined microstructure and enhanced mechanical properties in additively manufactured 17–4PH stainless steel. J Mater Process Technol 2024;328:118395. https://doi.org/10.1016/j.jmatprotec.2024.118395.
[10] Nezhadfar PD, Shrestha R, Phan N, Shamsaei N. Fatigue behavior of additively manufactured 17-4 PH stainless steel: synergistic effects of surface roughness and heat treatment. Int J Fatigue 2019;124:188–204. https://doi.org/10.1016/j.ijfatigue.2019.02.039.
[11] Lu J, Lu H, Xu X, Yao J, Cai J, Luo K. High-performance integrated additive manufacturing with laser shock peening –induced microstructural evolution and improvement in mechanical properties of Ti6Al4V alloy components. Int J Mach Tools Manuf 2020;148:103475. https://doi.org/10.1016/j.ijmachtools.2019.103475.
[12] Chi J, Cai Z, Wan Z, Zhang H, Chen Z, Li L, et al. Effects of heat treatment combined with laser shock peening on wire and arc additive manufactured Ti17 titanium alloy: Microstructures, residual stress and mechanical properties. Surf Coatings Technol 2020;396:125908. https://doi.org/10.1016/j.surfcoat.2020.125908.
[13] Lu Y, Sun GF, Wang ZD, Su BY, Zhang YK, Ni ZH. The effects of laser peening on laser additive manufactured 316L steel. Int J Adv Manuf Technol 2020;107:2239–49. https://doi.org/10.1007/s00170-020-05167-3.
[14] Jessy Michla JR, Ravikumar B, Ram Prabhu T, Siengchin S, Arul Kumar M, Rajini N. Effect of nitriding on mechanical and microstructural properties of Direct Metal Laser Sintered 17-4PH stainless steel. J Mater Res Technol 2022;19:2810–21. https://doi.org/10.1016/j.jmrt.2022.05.198.
[15] AlMangour B, Yang JM. Improving the surface quality and mechanical properties by shot-peening of 17-4 stainless steel fabricated by additive manufacturing. Mater Des 2016;110:914–24. https://doi.org/10.1016/j.matdes.2016.08.037.
[16] Lu HF, Xue KN, Xu X, Luo KY, Xing F, Yao JH, et al. Effects of laser shock peening on microstructural evolution and wear property of laser hybrid remanufactured Ni25/Fe104 coating on H13 tool steel. J Mater Process Technol 2021;291:117016. https://doi.org/10.1016/j.jmatprotec.2020.117016.
[17] Liu L, Wang J, Zhou J. Effects of laser shock peening on mechanical behaviors and microstructural evolution of brass. Vacuum 2018;148:178–83. https://doi.org/10.1016/j.vacuum.2017.11.024.
[18] Pathak S, Zulić S, Kaufman J, Kopeček J, Stránský O, Böhm M, et al. Post-processing of selective laser melting manufactured SS-304L by laser shock peening. J Mater Res Technol 2022:140138. https://doi.org/10.1016/j.jmrt.2022.07.014.
[19] Karthik D, Swaroop S. Electrochemical stability of laser shock peened 17-4 PH stainless steel. Opt Laser Technol 2019;120:105727. https://doi.org/10.1016/j.optlastec.2019.105727.
[20] Ozer M, Yılmaz O, Subasi L, Gunaydin A, Mert Bilgin G, Zulić S, et al. Enhancement of surface characteristics of additively manufactured γ-TiAl and IN939 alloys after laser shock processing. Opt Laser Technol 2024;170. https://doi.org/10.1016/j.optlastec.2023.110330.
[21] Lashgari HR, Kong C, Adabifiroozjaei E, Li S. Microstructure, post thermal treatment response, and tribological properties of 3D printed 17-4 PH stainless steel. Wear 2020;456–457:203367. https://doi.org/10.1016/j.wear.2020.203367.
[22] Ozyurek D, Nalcacioglu E, Cetinkaya K. Microstructure and wear behaviour of 17-4 precipitation hardening stainless steel with various Ti content. Powder Metall Met Ceram 2020;59:386–93. https://doi.org/10.1007/s11106-020-00172-3.
[23] Sanguedolce M, Zekonyte J, Alfano M. Wear of 17-4 PH stainless steel patterned surfaces fabricated using selective laser melting. Appl Sci 2021;11:9317. https://doi.org/10.3390/app11199317.
[24] Kc S, Nezhadfar PD, Phillips C, Kennedy MS, Shamsaei N, Jackson RL. Tribological behavior of 17–4 PH stainless steel fabricated by traditional manufacturing and laser-based additive manufacturing methods. Wear 2019;440–441:203100. https://doi.org/10.1016/j.wear.2019.203100.
[25] Srivatsav VR, Radhika N, Ragunath S, Niketh MS, Basak AK. Microstructural characterization and wear analysis of AlTiVZrMoCr HEA coating on SS410 steel by atmospheric plasma spraying. J Alloys Compd 2024;1008. https://doi.org/10.1016/j.jallcom.2024.176806.
[26] Vishnu V, Prabhu TR, Vineesh KP. Effect of hard anodizing and T6 heat treatment on the dry sliding wear behavior of AlSi10Mg fabricated by direct metal laser sintering. Wear 2025;564–565:205677. https://doi.org/10.1016/j.wear.2024.205677.
[27] Idusuyi N, Olayinka JI. Dry sliding wear characteristics of aluminium metal matrix composites: a brief overview. J Mater Res Technol 2019;8:3338–46. https://doi.org/10.1016/j.jmrt.2019.04.017.
[28] Mukherjee M, Sarkar P, Barman S, Mallisetty PK, Paleu V, Bhaumik S. Investigating the wear resistance of AISI 410/AISI 2205 hybrid weld cladding on annealed EN 8 medium carbon steel. Proc Inst Mech Eng Part J J Eng Tribol 2024;238:1373–92. https://doi.org/10.1177/13506501241255989.
[29] Muthu SM, Veeman D, Asokan V, Sathishkumar M, Vadivel Kannan L, Vignesh M, et al. Effect of heat treatment on tribological behavior of direct metal laser sintered alloy 718. iScience 2024;27:111415. https://doi.org/10.1016/j.isci.2024.111415.
[30] K H, Kumar SP, T P, Babu PD, N S. Investigating the effect of laser shock peening on the wear behaviour of selective laser melted 316L stainless steel. Opt Laser Technol 2023;162:109317. https://doi.org/10.1016/j.optlastec.2023.109317.
[31] Lashgari HR, Xue Y, Onggowarsito C, Kong C, Li S. Microstructure, tribological properties and corrosion behaviour of additively manufactured 17-4PH stainless steel: effects of scanning pattern, build orientation, and single vs. Double scan. Mater Today Commun 2020;25:101535. https://doi.org/10.1016/j.mtcomm.2020.101535.
[32] Radhika N, Sethupathi S, Ragunath S. Investigation on wear behavior of CoCrFeCuTi high-entropy alloy reinforced Ti6Al4V composites. Results Eng 2025;26:104832. https://doi.org/10.1016/j.rineng.2025.104832.
[33] Guennouni N, Barroux A, Grosjean C, Maisonnette D, Nivet E, Andrieu E, et al. Comparative study of the microstructure between a laser beam melted 17-4PH stainless steel and its conventional counterpart. Mater Sci Eng A 2021;823:141718. https://doi.org/10.1016/j.msea.2021.141718.
[34] Zai L, Zhang C, Wang Y, Guo W, Wellmann D, Tong X, et al. Laser powder bed fusion of precipitation-hardened martensitic stainless steels: a review. Metals 2020;10:255. https://doi.org/10.3390/met10020255.

[35] Nezhadfar PD, Shrestha R, Phan N, Shamsaei N. Fatigue behavior of additively manufactured 17-4 PH stainless steel: synergistic effects of surface roughness and heat treatment. Int J Fatigue 2019;124:188–204. https://doi.org/10.1016/j.ijfatigue.2019.02.039.
[36] Liu J, Liu H, Chen P, Hao J. Microstructural characterization and corrosion behaviour of AlCoCrFeNiTix high-entropy alloy coatings fabricated by laser cladding. Surf Coatings Technol 2019;361:63–74. https://doi.org/10.1016/j.surfcoat.2019.01.044.
[37] Gill AS, Telang A, Ye C, Mannava SR, Qian D, Vasudevan VK. Localized plastic deformation and hardening in laser shock peened Inconel alloy 718SPF. Mater Charact 2018;142:15–26. https://doi.org/10.1016/j.matchar.2018.05.010.
[38] Lan L, Xin R, Jin X, Gao S, He B, Rong Y, et al. Effects of laser shock peening on microstructure and properties of Ti-6Al-4V titanium alloy fabricated via selective laser melting. Materials 2020;13:1–11. https://doi.org/10.3390/MA13153261.
[39] Umapathi A, Swaroop S. Mechanical properties of a laser peened Ti-6Al-4V. Opt Laser Technol 2019;119:105568. https://doi.org/10.1016/j.optlastec.2019.105568.
[40] Pour-Ali S, Tavangar R, Hejazi S. Effect of micro-shot peening on microstructure and fluoride-induced corrosion performance of AISI 904L superaustenitic stainless steel. Mater Today Commun 2023;36:106682. https://doi.org/10.1016/j.mtcomm.2023.106682.
[41] Ragunath S, Radhika N, Aravind Krishna S, Jeyaprakash N. Enhancing microstructural, mechanical and tribological behaviour of AlSiBeTiV high entropy alloy reinforced SS410 through friction stir processing. Tribol Int 2023;188:108840. https://doi.org/10.1016/j.triboint.2023.108840.
[42] Samuel SC, M A, T RP. High temperature dry sliding wear behaviour of laser powder bed fused Inconel 718. Addit Manuf 2020;34:101279. https://doi.org/10.1016/j.addma.2020.101279.
[43] Sarkar S, Kumar CS, Nath AK. Effect of different heat treatments on mechanical properties of laser sintered additive manufactured parts. J Manuf Sci Eng 2017;139. https://doi.org/10.1115/1.4037437.
[44] Praveenkumar K, Vishnu J, Samuel SC, Gopal V, Arivarasu M, Lackner JM, et al. High temperature dry sliding wear behaviour of selective laser melted Ti-6Al-4V alloy surfaces. J Mater Process Technol 2024;329:118439. https://doi.org/10.1016/j.jmatprotec.2024.118439.
[45] Guo Y, Wang S, Liu W, Sun Z, Zhu G, Xiao T. Effect of laser shock peening on tribological properties of magnesium alloy ZK60. Tribol Int 2020;144:106138. https://doi.org/10.1016/j.triboint.2019.106138.
[46] Tong ZP, Ren XD, Zhou WF, Adu-Gyamfi S, Chen L, Ye YX, et al. Effect of laser shock peening on wear behaviors of TC11 alloy at elevated temperature. Opt Laser Technol 2019;109:139–48. https://doi.org/10.1016/j.optlastec.2018.07.070.



https://dspace.org/

Evaluation of high-temperature wear behaviour of selective laser melted 17-4 PH stainless steel through laser shock peening

Pradeep Kumar, S.; Radhika, N.; Dinesh Babu, P.; Ram Prabhu, T.; Gautam, Jaiprakash ...

2025-07-01
Elsevier
https://doi.org/10.1016/j.jmrt.2025.07.164
Pradeep Kumar S, Radhika N, Dinesh Babu P, et al., (2025) Evaluation of high-temperature wear behaviour of selective laser melted 17-4 PH stainless steel through laser shock peening. Journal of Materials Research and Technology, Volume 37, July 2025, pp. 5265-5282.

Downloaded from a DSpace repository. https://dspace.org/